

EPISODE III: The Nested Jet/Outflow Morphology of EC 53 Revealed by JWST and ALMA

SEONJAE LEE ,¹ JEONG-EUN LEE ,^{1,2} CHUL-HWAN KIM ,¹ SEOKHO LEE ,³ DOUG JOHNSTONE ,^{4,5}
 GREGORY J. HERCZEG ,^{6,7} JOEL GREEN ,⁸ LOGAN FRANCIS ,⁹ YAO-LUN YANG ,¹⁰ HYUNDONG LEE ,¹ AND
 NAGAYOSHI OHASHI ,¹¹

¹Department of Physics and Astronomy, Seoul National University, 1 Gwanak-ro, Gwanak-gu, Seoul 08826, Republic of Korea

²SNU Astronomy Research Center, Seoul National University, 1 Gwanak-ro, Gwanak-gu, Seoul 08826, Republic of Korea

³Korea Astronomy and Space Science Institute, 776 Daedeok-daero, Yuseong-gu, Daejeon 34055, Republic of Korea

⁴NRC Herzberg Astronomy and Astrophysics, 5071 West Saanich Rd, Victoria, BC V9E 2E7, Canada

⁵Department of Physics and Astronomy, University of Victoria, 3800 Finnerty Rd, Elliot Building, Victoria, BC V8P 5C2, Canada

⁶Kavli Institute for Astronomy and Astrophysics, Peking University, Yiheyuan Lu 5, Haidian Qu, 100871 Beijing, People's Republic of China

⁷Department of Astronomy, Peking University, Yiheyuan 5, Haidian Qu, 100871 Beijing, People's Republic of China

⁸STScI, 3700 San Martin Drive, Baltimore, MD 21218, USA

⁹Leiden Observatory, Leiden University, PO Box 9513, 2300 RA Leiden, The Netherlands

¹⁰Star and Planet Formation Laboratory, Pioneering Research Institute, RIKEN, 2-1 Hirosawa, Wako, Saitama, 351-0198, Japan

¹¹Academia Sinica Institute of Astronomy & Astrophysics, 11F of Astronomy-Mathematics Building, AS/NTU, No. 1, Sec. 4, Roosevelt Rd., Taipei 10617, Taiwan, R.O.C.

ABSTRACT

We present an extensive study of the structure and kinematics of the jet and outflow of EC 53, a Class I protostar with a quasi-periodic variability, using combined James Webb Space Telescope (JWST) and Atacama Large Millimeter/submillimeter Array (ALMA) observations. ALMA continuum observations resolve a compact disk with a radius of $\sim 0.14''$ (60 au). Scattered light from the outflow cavity is prominent in the short-wavelength NIRCam and NIRSpec observations, revealing only the southeast nearside lobe. We detected 27 H₂ emission lines tracing a narrow, cone-shaped structure within the outflow cavity. A high-velocity ionized jet is detected in several forbidden atomic lines, characterized by a position angle of 142°, an opening angle of 1.4°, and an estimated geometric launching radius of at most ~ 40 au. Mid-infrared CO ro-vibrational emission lines, stronger in the P-branch, show a similar distribution to the H₂ emission and are likely to originate from hot gas within the outflow cavity. CO and C₂H emission lines detected by ALMA trace slower, colder outflow components and cavity walls. The spatial and kinematic stratification between the hot atomic and molecular components and the colder molecular gas is consistent with predictions from MHD disk wind models, although envelope material entrained by a wide-angle wind or jet may also contribute. Our analysis highlights the powerful synergy between JWST and ALMA in advancing the understanding of protostellar jets and outflows across multiple spatial and physical scales.

1. INTRODUCTION

The formation of stars is initiated by the gravitational collapse of dense cores within molecular clouds (F. H. Shu et al. 1987; S. Terebey et al. 1984). As these cores collapse, conservation of angular momentum increases the rotational velocity, which, if unregulated, can bring the nascent star close to the so-called break-up limit, where centrifugal forces exceed the gravitational pull (P. Bodenheimer 1995). This scenario underscores the

classical angular momentum problem in star formation; without efficient angular momentum removal, protostars cannot form (C. F. McKee & E. C. Ostriker 2007). This issue is mitigated through the combined roles of two key components: accretion disks and bipolar ejections. The disk acts as a reservoir of angular momentum, allowing mass transport toward the protostar, while jets and outflows serve as channels for expelling excess angular momentum from the system (A. Frank et al. 2014; R. E. Pudritz et al. 2007).

Bipolar ejection phenomena are typically divided into high-velocity, well-collimated jets and lower-velocity, wide-angle outflows (H. G. Arce et al. 2007; A. Frank

et al. 2014). Jets are often associated with shock features such as knots and bow shocks and are believed to originate in the inner regions of the star-disk system, near the dust sublimation radius. These jets are traced by atomic or ionic emission lines, including [Fe II], [Ni II], and [Ne II] (see review by J. Bally 2016; E. F. van Dishoeck et al. 2025). Molecular jets, which are more common in deeply embedded Class 0 sources, can be traced with molecular lines such as CO, SiO, SO, and ro-vibrationally excited H₂ (M. Tafalla et al. 2000; N. Hirano et al. 2010; C.-F. Lee et al. 2017; A. Caratti o Garatti et al. 2024). On the other hand, outflows are typically traced with cooler molecular species, such as purely rotational H₂, CO, H₂CO, and CH₃OH (R. Bachiller 1996; J. K. Jørgensen et al. 2007; L. Tychoniec et al. 2021).

Multiple theoretical models have been proposed to explain the launching and collimation of jets and outflows (R. E. Pudritz & T. P. Ray 2019; T. P. Ray & J. Ferreira 2021). The stellar wind model proposes that winds are launched directly from the stellar surface, carrying away angular momentum and regulating stellar spin (S. Matt & R. E. Pudritz 2005, 2008). The X-wind model suggests that wide-angle high-velocity winds power outflows and originate near the corotation radius, where the stellar magnetosphere truncates the disk (F. Shu et al. 1994). These models emphasize angular momentum removal near the inner disk, allowing mass to reach the protostar without a catastrophic increase in angular momentum, but leave unexplained the process by which accretion through the disk occurs. The magnetohydrodynamic (MHD) disk wind model offers a promising solution by enabling angular momentum extraction over a broad radial extent of the disk and creating an inward flow of material through the disk (R. D. Blandford & D. G. Payne 1982; J. Ferreira et al. 2006; X.-N. Bai & J. M. Stone 2013).

MRI (magnetorotational instability) has also been identified as a key mechanism for driving turbulence and accretion in ionized regions of the disk (S. A. Balbus & J. F. Hawley 1991). MRI is efficient in hot, ionized regions but becomes ineffective in the colder, neutral midplane of the outer disk—known as the ‘dead zone’ (G. R. J. Lesur 2021; I. Pascucci et al. 2023). In the dead zone, MHD disk winds are suggested as being dominant. Other outflow-driving mechanisms, such as photoevaporative (PE) disk winds (B. Ercolano & I. Pascucci 2017), wind-driven entrainment (C.-F. Lee et al. 2000; L. Liang et al. 2020), and jet-driven entrainment (M. Rabenahary et al. 2022), may also operate simultaneously, but are unlikely to play a major role in enabling disk accretion.

Observationally, the synergy between ALMA and JWST provides a comprehensive, multi-wavelength view of protostellar jet and outflow systems. ALMA excels at tracing low-temperature molecular lines with high spatial and spectral resolution, revealing velocity gradients across outflows that are often interpreted as signatures of jet rotation or magnetically driven disk winds (C.-F. Lee et al. 2017, 2018; A. de Valon et al. 2020; J. A. López-Vázquez et al. 2024). Complementing this, JWST’s NIRSpec/IFU and MIRI/MRS instruments probe hot gas and ionic emission, uncovering the fine structure of jets and outflows in unprecedented detail (T. P. Ray et al. 2023; D. Harsono et al. 2023; M. Narang et al. 2024; B. Nisini et al. 2024; K. D. Assani et al. 2024; A. Caratti o Garatti et al. 2024; M. Narang et al. 2025; M. G. Navarro et al. 2025). With both facilities offering sub-arcsecond spatial resolution, their combined capabilities enable a deeper understanding of the physical conditions, dynamics, and morphology of the protostellar outflow environment (V. Delabrosse et al. 2024; L. Tychoniec et al. 2024; Y. Okuda et al. 2025; E. F. van Dishoeck et al. 2025).

To leverage this synergy, we conducted both ALMA and JWST observations of EC 53 (V371 Ser), a quasi-periodically variable Class I protostar (K. W. Hodapp et al. 2012; Y.-H. Lee et al. 2020) located in the Serpens Main star-forming region (d=436 pc; G. N. Ortiz-León et al. 2017). EC 53 is known to drive a well-developed bipolar outflow oriented northwest (redshifted) to southeast (blueshifted), and harbors a compact disk with a radius of approximately 100 au. The southeastern side of the disk is oriented toward the observer and is seen through the blueshifted outflow cavity, along which scattered near-IR light has been observed (K. W. Hodapp et al. 2012). Previous ALMA observations suggest a minimum central mass of $\sim 0.3 \pm 0.1 M_{\odot}$ and a disk inclination of $34^\circ.8 \pm 2^\circ.1$ (0° is face-on; S. Lee et al. 2020).

In this paper, we present the results of our coordinated ALMA and JWST observations aimed at characterizing the jet and outflow structures in EC 53 through a range of diagnostic tracers. This paper is the third in a series of papers on the JWST program, *EPISODE: EC 53, the only known Periodically variable Infant Star to chase the Outburst in the next Dynamical Event*. Paper I (J.-E. Lee et al. 2026) highlights silicate crystallization in the inner disk. Paper II (Seokho Lee et al., submitted) analyzes the variability of gas absorption lines. Paper IV (Kim et al., submitted) focuses on the ice absorption in the envelope.

Section 2 details the observational setup and data reduction procedures. In Section 3, we describe the morphological components of the jet and outflow system.

Section 4 presents the derived physical properties, and Section 5 explores their implications for the origin and launching mechanisms of the observed outflows. We conclude with a summary of our main findings in Section 6.

2. OBSERVATION & DATA REDUCTION

2.1. ALMA

To trace the outflow and its cavity walls, we used molecular line observations from ALMA. The CO 2–1 line was used to probe both large- and small-scale outflows, combining data from Cycle 7 with a beam size of $\sim 1''$ (Project ID: 2019.1.01792.S, PI: Diego Mardones; [C.-H. Hsieh et al. 2024](#)) and Cycle 9 with a beam size of $\sim 0.1''$ (Project ID: 2022.1.00800.S, PI: Seokho Lee). To trace the outflow cavity walls, we used Cycle 4 data with a beam size of $0.3''$ (Project ID: 2016.1.01304.T, PI: Jeong-Eun Lee; [S. Lee et al. 2020](#)). For further details on the Cycle 4 and Cycle 7 observations, we refer the reader to [S. Lee et al. \(2020\)](#) and [C.-H. Hsieh et al. \(2024\)](#), respectively. Table 1 summarizes the ALMA observations used in this study.

The Cycle 9 line and continuum observations were conducted on 2023 May 24 and 2023 September 1, respectively. The observations covered baselines ranging from 27.5 m to 3.6 km with 43 12-m antennas for the former, and from 83.1 m to 15.2 km with 41 12-m antennas for the latter. The on-source integration times were 43.1 minutes and 46.1 minutes, respectively. The data were initially calibrated using the CASA 6.1.1.15 pipeline ([J. P. McMullin et al. 2007](#)). The quasar J1924–2914 was used as the bandpass and amplitude calibrator, and the nearby quasar J1851+0035 served as the phase calibrator. To improve image quality of the molecular line data, the continuum image was generated using line-free channels, followed by three rounds of phase self-calibration with solution intervals of 300 s, 150 s, and 56.5 s ('int'), respectively. A final round of amplitude self-calibration was also performed. The CO 2–1 image was cleaned using natural weighting, with and without a UV tapering of $0.2''$. The continuum image was cleaned using Briggs weighting with a robust parameter of 0.5, yielding a beam size of $0.02''$.

2.2. JWST

The NIRSpec IFU and MIRI MRS observations of EC 53 during the burst phase were obtained as part of the General Observer (GO) program 3477 (PI: Jeong-Eun Lee) on May 10, 2024. The NIRSpec IFU observations cover a wavelength range from 1.7 to $5.3\mu\text{m}$ with a resolving power of 2700, while the MIRI MRS observations cover a wavelength range from 4.9 to $27.9\mu\text{m}$ ($R=1500-3500$). These observations enable the investigation of the

jet/outflow using various atomic and molecular lines. A detailed description of the observations and data reduction procedures is provided in [J.-E. Lee et al. \(2026\)](#) for MIRI and Seokho Lee et al. (submitted; Paper II) for NIRSpec.

Supplementary JWST NIRCam images covering EC 53 were obtained from the Cycle 1 GO program 1611 (PI: Klaus M. Pontoppidan). [J. D. Green et al. \(2024\)](#) presents four images taken with different medium-band filters: F140M, F210M, F360M, and F480M. Each filter covers various emission lines known to trace protostellar outflows. The F480M filter includes H₂ 0–0 S(9) at $4.6947\mu\text{m}$, [Fe II] at $4.8891\mu\text{m}$, and the CO fundamental line forest. The F360M filter contains high energy transitions of H₂ 0–0 lines, while the F210M filter covers the H₂ 1–0 S(1) $2.1218\mu\text{m}$ line. The F140M filter is primarily dominated by scattered light. For detailed observation and preprocessing strategy of the archival NIRCam data, we refer to [J. D. Green et al. \(2024\)](#).

2.2.1. Spectral Extraction and Flux Calibration

While the basic data reduction and astrometric correction methods are described in Papers I and II, here we outline the additional steps used to extract spectra from individual spaxels. First, we applied a custom hot/cold pixel reduction method to remove residual hot and cold pixels that remained after processing with the JWST Calibration Pipeline. Further details on this method are provided in Appendix B.

For comparison, we extracted representative 1D spectra at the position of the central source and at a selected outflow position coincident with the mid-IR CO emission peak, using an aperture radius of $0.4''$. The resulting spectra are shown in Figure 1; the top two panels correspond to the central source, and the bottom two panels to the outflow position. There are small discrepancies in flux levels between different spectral bands — this is a known issue in JWST data, previously reported in the literature (e.g., [Y.-L. Yang et al. 2022](#); [M. L. van Gelder et al. 2024](#); [B. Nisini et al. 2024](#)). To correct for this, we scaled each band to match the flux level of MIRI channel 1. However, the mismatch between the shortest wavelength in MIRI and the longest in NIRSpec is much larger than in other subbands, and the scale factor varies across positions, ranging from approximately 0.8 to 6. We do not apply scale factors between NIRSpec and MIRI, but perform analysis separately for each instrument. Additional details about the flux discrepancies are provided in Appendix C.

All spectra used in this study were further corrected for residual fringe patterns using the `fit_residual_fringes_1d` routine, a post-pipeline 1D

Table 1. Description of the ALMA data used in this work.

Type	Spectral Resolution	Beam size	σ [mJy beam $^{-1}$]	Program
CO J=2–1	61 kHz	0.90'' \times 0.69''	18.9	2019.1.01792.S
C ₂ H N=4–3	244 kHz	0.31'' \times 0.30''	2.87	2016.1.01304.T
Continuum	-	0.018'' \times 0.015''	0.043	2022.1.00800.S
CO J=2–1	122 kHz	0.12'' \times 0.10''	1.68	2022.1.00800.S
CO J=2–1 ^a	384 kHz	0.31'' \times 0.31''	1.97	2022.1.00800.S

^a UV Tapered.

fringe correction method. Near the central source, absorption features from simple ices and silicates are clearly visible. In the outflow region, absorption features persist, but numerous emission lines from various atomic and molecular species are also present.

2.2.2. Reduction of Emission Lines

We adopted a method similar to that of K. D. Assani et al. (2024) to recover the line emission distribution. For each spaxel, we defined the channels with a velocity between -300 km s^{-1} and 300 km s^{-1} as the ‘emission channels’, and channels between -1000 km s^{-1} and 1000 km s^{-1} , excluding the emission channels, as the ‘continuum channels’. A quadratic function was fitted to the continuum channels to estimate the continuum level at each spaxel. We used the median value as the constant continuum level for spaxels for which a valid quadratic fit could not be obtained.

Using the continuum fit at each spaxel, we generated a continuum cube and a continuum-subtracted line cube for each emission line. From the line cube, we produced integrated-intensity and peak-intensity maps. We masked out spaxels with a signal-to-noise ratio (SNR) below 3 and manually excluded spaxels with unphysically high intensities. The noise level for each spaxel was estimated with the root-mean-square (RMS) of the residuals in the continuum channels, and SNR was then calculated as the ratio of the peak intensity to the noise. Figure 2 shows the full process for generating the H₂ 3.235 μm emission map.

3. RESULTS

In this section, we describe five distinct emission structures observed in EC 53: the envelope cavity and central source detected in the continuum, wide-angle H₂ outflow, collimated ionic jet, hot mid-IR CO emission, and ALMA outflow tracers. Figure 3 shows a schematic view of the jet and outflow system for EC 53.

3.1. Envelope Cavity and Central Source detected in Continuum

The scattered light from the central source appears as continuum emission within the outflow cavity at short wavelengths. However, since the dust scattering cross-section decreases with increasing wavelength, the continuum morphology varies significantly across wavelengths.

The top panels of Figure 4 show the continuum emission at different wavelengths as observed with NIRSpec and MIRI. In the image of the shortest wavelength (1.7 μm), the most prominent feature is the wide outflow cavity. Only the southeast cavity, which corresponds to the blue-shifted lobe facing the observer, is visible. No strong emission is detected near the central source. At 2.2 μm , the outflow cavity remains visible, but the brightest point of emission shifts northward toward the central source. In contrast, at the longer wavelengths of 4.8 μm and 10 μm , outflow structures are no longer visible, as scattered light becomes negligible. Additionally, the centrally peaked emission is unresolved at these wavelengths because the PSF full width at half maximum (FWHM) exceeds the source size.

This wavelength-dependent trend is also seen in the photometric images. The bottom panels of Figure 4 show JWST NIRCam images, which cover a larger field of view than a single NIRSpec cube slice (outlined in white dashed lines). The outflow cavity extends farther from the central source in these images. Comparing the NIRCam images, it is clear that the outflow and outflow cavity features dominate at shorter wavelengths, whereas the emission from the central source is prominent at longer wavelengths. In the F360M and F480M images, diffraction patterns from the central source are visible. Although scattered light from the cavity remains, it is significantly dominated by emission from the central source.

High angular resolution ALMA observations resolve the central source with a beam size of $\sim 0.02''$. The ALMA continuum shown in Figure A1 and the top panels of Figure 4 trace the central protostar and its protoplanetary disk. We fitted the disk with a two-

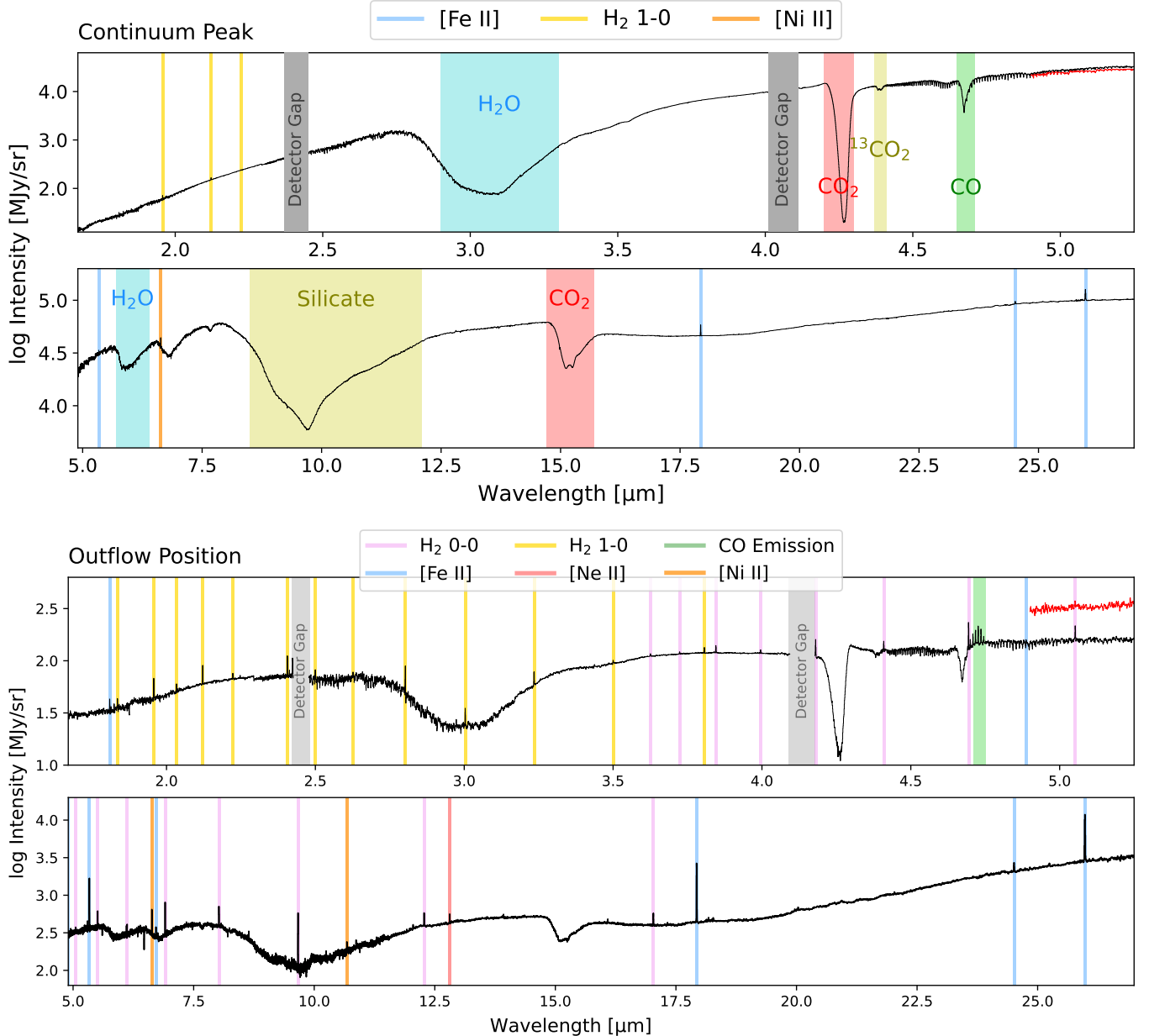


Figure 1. Near through mid-IR spectra toward EC 53 extracted from two different positions using a $0.4''$ aperture. The top two panels show the spectrum obtained at the ALMA continuum peak (18:29:51.175, +01:16:40.324), with the NIRSpec spectrum on top and the MIRI spectrum below. The bottom two panels show the same for an outflow position (18:29:51.26, +01:16:38.80), which corresponds to the mid-IR CO emission peak. Detector gaps, major ice absorption features, and emission lines are highlighted in various colors. In both NIRSpec panels, the overlapping portion of the MIRI spectrum is overplotted in red for comparison.

dimensional Gaussian using the `imfit` task in CASA. The central position of the continuum is at $\alpha = 18^{\text{h}}29^{\text{m}}51.17537^{\text{s}}$, $\delta = 1^{\text{d}}16^{\text{m}}40.32810^{\text{s}}$ (J2000). After deconvolving the beam, the fitted disk has a semimajor axis of 142.5 ± 2.5 mas (62.1 ± 1.1 au), a semiminor axis of 121.0 ± 2.1 mas (52.8 ± 0.9 au), and a position angle of $60.6 \pm 4.4^\circ$. Assuming a circular disk, the resulting inclination derived from the axis ratio is $31.9 \pm 3.2^\circ$. These

values are consistent with previous estimates from lower-resolution ALMA data (S. Lee et al. 2020). The MIRI emission peak coincides with the ALMA continuum.

3.2. Wide Angle Outflow traced by H_2

A total of 27 H_2 emission lines are detected with $S/N > 3$ from our observations. Table D1 lists all the lines detected. The H_2 line information is compiled from the

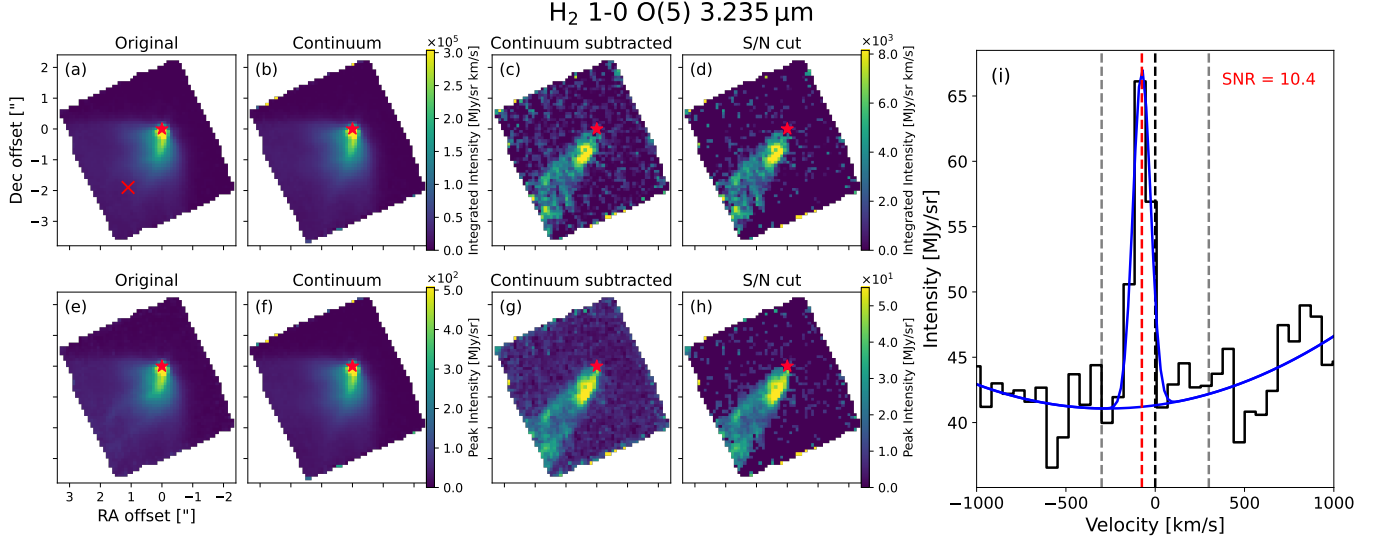


Figure 2. Reduction process of the H_2 $3.235 \mu\text{m}$ line emission. (a–d) Integrated intensity maps at each stage of the reduction: (a) after hot pixel removal and flux calibration; (b) quadratic baseline fitting result; (c) after continuum subtraction; and (d) after applying a signal-to-noise (S/N) cut of 3. The image center is shifted southeastward to better display the outflow structure. (e–h) Corresponding peak intensity maps for each stage, respectively. The ALMA continuum center is marked with a red star. (i) Spectrum at the location marked with a red cross in panel (a). Gray vertical dashed lines indicate velocities of -300 km s^{-1} and $+300 \text{ km s}^{-1}$, used to define the emission channels. The blue line shows the fitted continuum and Gaussian profile. The red vertical dashed line indicates the Gaussian centroid, which is blueshifted relative to the barycentric velocity of the source (-8.9 km s^{-1} , thick black dashed line).

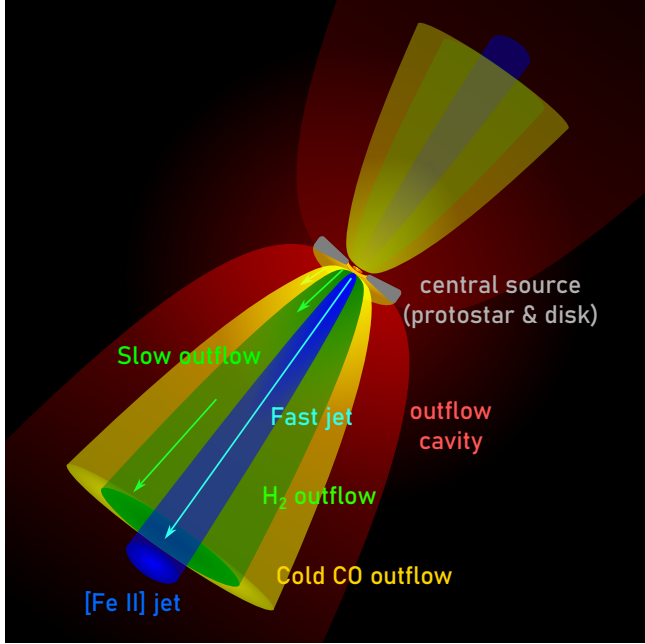


Figure 3. Schematic view of EC 53, highlighting each component analyzed in this work.

HITRAN database (I. Gordon et al. 2026). Both vibrational transitions ($v=0-0$ and $1-0$) are detected from the O, Q, and S branches, with upper energy levels reaching as high as 20,000 K. No $v=2-1$ lines or HD lines are detected with $\text{S/N} > 3$.

The H_2 emission shows a cone-like morphology, narrower than the outflow cavity traced by scattered light, as shown in Figure 2. Figures D5 and D6 present the integrated intensity maps of each H_2 line obtained with NIRSpec and MIRI, respectively. Further discussion on the morphology and physical parameters of the H_2 outflow is discussed in Sections 4.1 and 4.2.

3.3. Ionic Jet

Several forbidden atomic lines, including $[\text{Fe II}]$, $[\text{Ne II}]$, and $[\text{Ni II}]$, are detected. No hydrogen recombination, helium, or argon lines are detected. Table D2 lists all the atomic lines detected in our observations. Line information is from the NIST Atomic Spectra Database (A. Kramida et al. 2023).

Figure D7 shows the continuum-subtracted integrated intensity maps of the detected atomic emission lines. All atomic lines exhibit a similar collimated structure aligned along the blueshifted side of the outflow, regardless of the species. Two $[\text{Fe II}]$ lines (17.94 and $25.99 \mu\text{m}$) also show redshifted emission on the northeast side.

3.4. Hot CO Emission and Absorption

The spectral resolution of NIRSpec and MIRI is sufficient to resolve individual lines within the CO forest around $4.7 \mu\text{m}$ (see Figure 5). Numerous lines from various vibrational bands ($^{12}\text{CO } v=1-0$, $v=2-1$, $^{13}\text{CO } v=1-0$) are detected, alongside CO ice absorption and

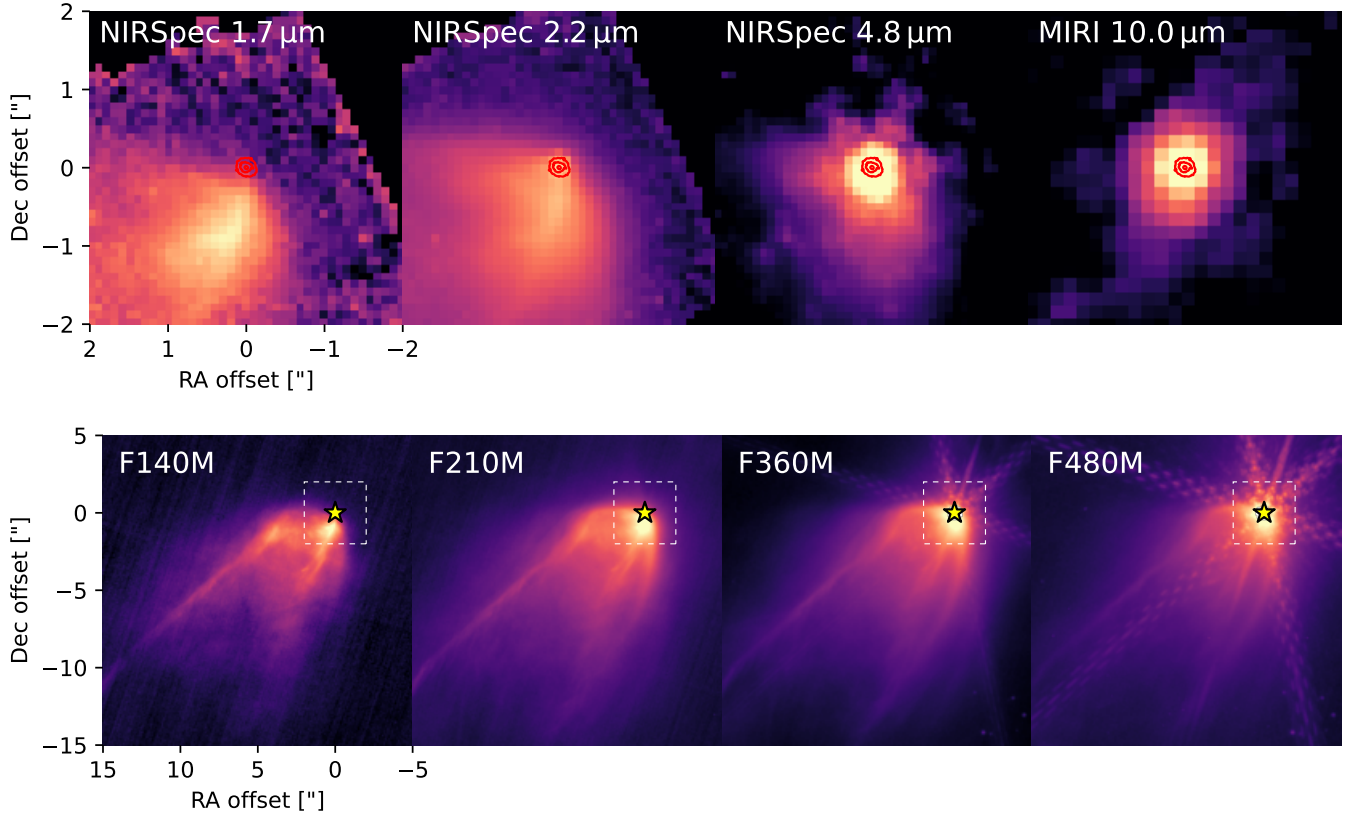


Figure 4. (Top) Continuum of EC 53 observed with JWST NIRSpec and MIRI at different wavelengths. The ALMA continuum is overlaid as red contours. (Bottom) Scattered light around EC 53 imaged by JWST NIRCam in different filters. A white dashed square indicates the area shown in the top panels. The position of the central source is marked with a yellow star. The ALMA continuum peak coincides with the peak positions in all images at wavelengths longer than $2.1\mu\text{m}$. The colorscale is logarithmic across all panels to accentuate faint details.

H_2 and $[\text{Fe II}]$ emission lines. The spectra extracted from the central source position show that all CO lines are in absorption. A detailed analysis of these absorption features will be presented in a separate study (Seokho Lee et al., submitted). On the contrary, in the spectra from the outflow, the ^{12}CO $v=1-0$ P-branch transitions from $J=4$ to $J=11$ appear in emission, while the R-branch lines and other CO bands remain in absorption. Figure 6 shows the integrated intensity map of the ^{12}CO $v=1-0$ P(8) line at $4.7359\mu\text{m}$. Near the central source, the CO line shows in absorption. However, a distinct area southeast of the central source exhibits emission. The origin of this emission and P-R asymmetry is discussed further in Section 4.5.

3.5. ALMA Outflow Tracers

Figure 7 presents the integrated intensity maps of CO and C_2H in EC 53. The CO outflow appears as two lobes extending widely ($>10''$) on both sides of the central protostar. An additional extended emission is present in the same region as the redshifted lobe. This emission is also detected in the NIRCam images and has been identified

as associated with S68Nb2 (J. D. Green et al. 2024). Its blueshifted velocity further supports the interpretation that it is unrelated to the EC 53 outflow.

Due to the high spatial resolution of the CO observations (beam size $\sim 0.1''$), large-scale structures ($>1''$) are partially resolved out. Nevertheless, the overall morphology of the outflow is consistent with that seen in lower-resolution data. As reported in Figure 3 of S. Lee et al. (2020), C_2H traces the outflow cavity walls, which are broader than the CO outflow. C_2H can be enhanced by UV photons (A. Fuente et al. 1993), while it can be destroyed by gas phase reactions with H_2 in the warm envelope (Y. Aikawa et al. 2012). This explains why C_2H is typically observed along cavity walls (L. Tychoniec et al. 2021). The spatial correlation between the C_2H emission and the near-IR scattered light supports the interpretation that the scattered light traces the outflow cavity structure.

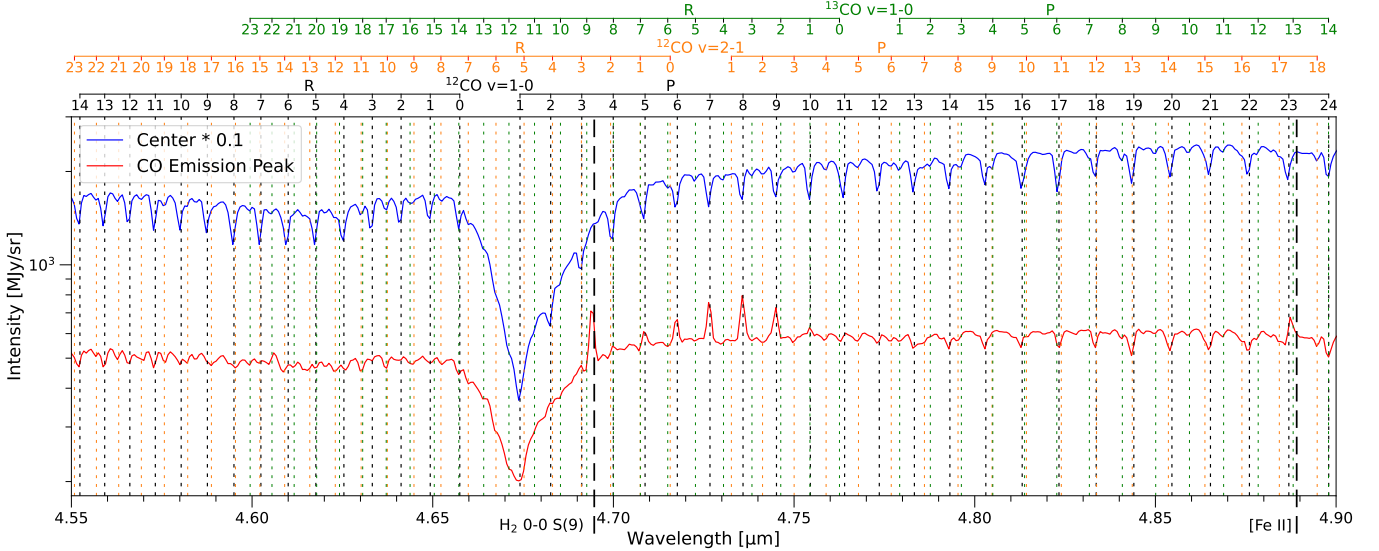


Figure 5. Spectra between $4.55\text{ }\mu\text{m}$ and $4.90\text{ }\mu\text{m}$ for the central source (blue) and CO emission peak (red). Both spectra are extracted using a $0.3''$ aperture. The wavelengths of the $^{12}\text{CO } v=1-0$, $v=2-1$, and $^{13}\text{CO } v=1-0$ transitions are marked with black, green, and orange dotted lines, respectively. Two transitions from other species, $\text{H}_2 0-0 \text{ S}(9)$ and $[\text{Fe II}]$, are indicated with black dashed lines. The line positions are shown in the rest frame without applying velocity shift corrections.

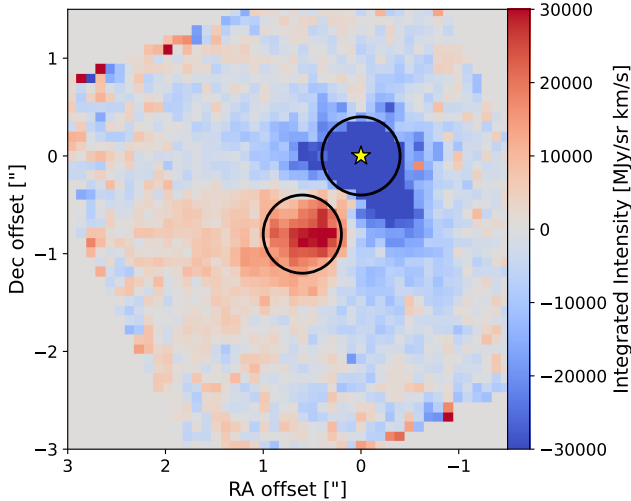


Figure 6. Integrated intensity map of the $^{12}\text{CO } v=1-0 \text{ P}(8)$ line. The central region appears in absorption while the surrounding regions exhibit emission. The apertures used for extracting the spectra of Figures 1 and 5 are marked with black circles. The ALMA center position is marked with a yellow star.

4. ANALYSIS

4.1. H_2 Emission Morphology

Figure 8 shows transverse cut profiles for various H_2 transitions. Since the H_2 transitions are scattered over a large range of wavelengths from ro-vibrational lines at $\sim 2\text{ }\mu\text{m}$ to $v=0-0 \text{ S}(1)$ at $17.035\text{ }\mu\text{m}$, it is critical to account for the wavelength dependent PSF before comparing the line widths. The PSF FWHM as a function

of wavelength for MIRI is calculated from D. R. Law et al. (2023):

$$\theta_\lambda = 0.033(\lambda/\text{micron}) + 0.106''. \quad (1)$$

The PSF FWHM of NIRSpec IFU is not well constrained and differs by dither patterns. In this work, we use a conservative constant value of $0.15''$ (F. D'Eugenio et al. 2024). We deconvolve the observed line width using the following equation:

$$\theta_{\text{Real}} = \sqrt{\theta_{\text{Apparent}}^2 - \theta_{\text{PSF}}^2}. \quad (2)$$

After deconvolving the PSF from the observed line profile, there is a trend between excitation energy and spatial extent for the majority of the lines. Excluding the $v=0-0 \text{ S}(1)$ line with the lowest energy, there is a decreasing trend in line width with increasing upper energy. The lower energy lines ($E_u < 5000\text{ K}$) show a decrease in width from $\sim 1.7''$ to $\sim 1.1''$, while the higher energy lines have a similar width of $\sim 1.1''$. This suggests a nested structure, where more highly excited gas is more centrally concentrated.

4.2. H_2 Emission Excitation Diagram Analysis

Since multiple emission lines from the same species are detected, we perform an excitation diagram analysis to derive the physical properties at each position of the outflow. Assuming that H_2 in the outflow is in local thermodynamical equilibrium (LTE) and that all lines are optically thin, the column density, excitation

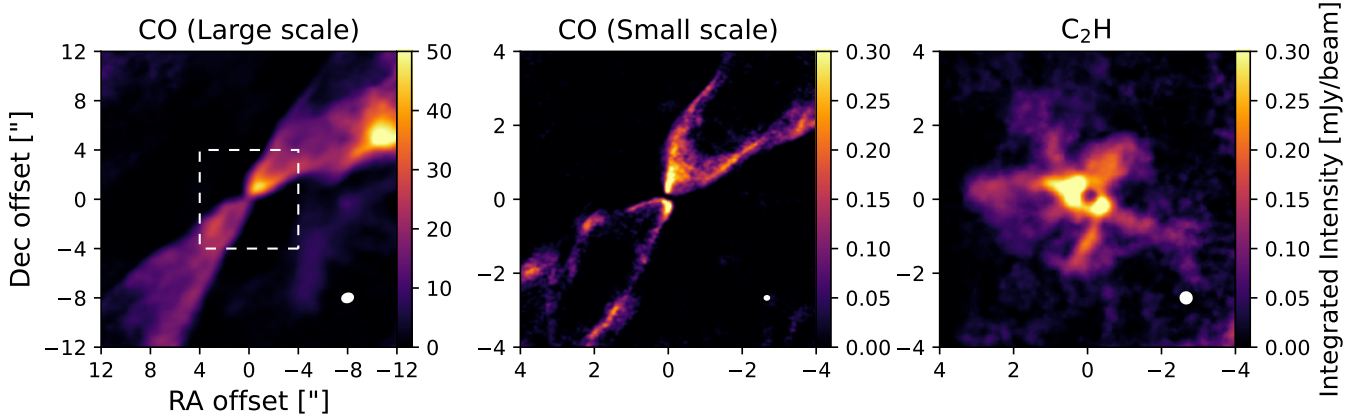


Figure 7. Integrated intensity maps of CO and C₂H from ALMA. A white ellipse indicates the beam size for each map. The leftmost panel covers a larger field of view (24'' \times 24''), while the other panels show zoomed-in regions (8'' \times 8''). The white dashed box in the leftmost panel outlines the area shown in the smaller panels.

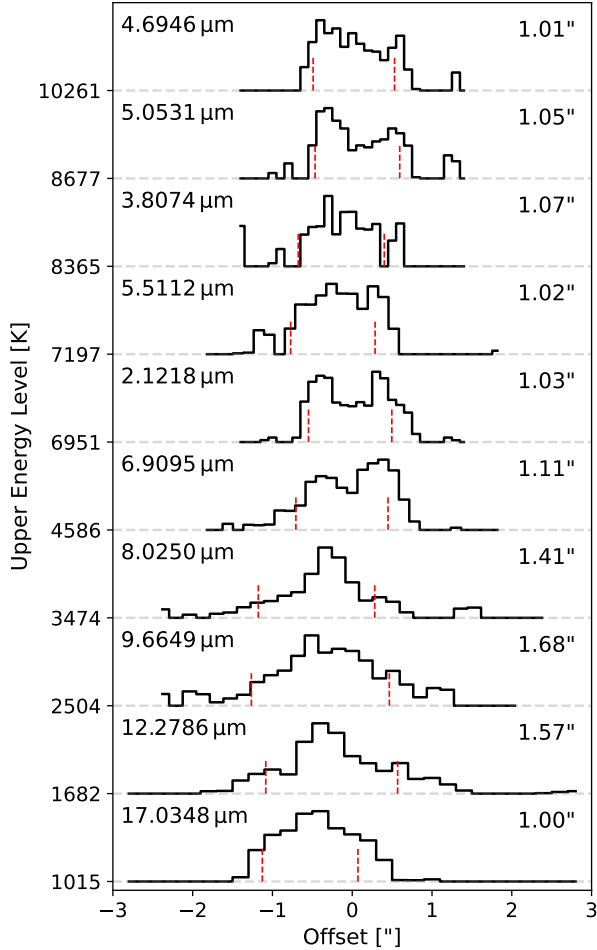


Figure 8. Normalized transverse cut profiles across the blueshifted outflow of EC 53 at 2'' distance from the central source for each of the H₂ transitions. For each transition, the observed FWHM is marked with red dashed lines, and the PSF deconvolved FWHM is written in the upper right corner.

temperature, and extinction can be obtained using the following equations:

$$N_i = \frac{4\pi}{hcA_{ij}} \int I_\nu dV, \quad (3)$$

$$\ln \left(\frac{N_i}{g_i} \right) = \ln \left(\frac{N}{Q} \right) - \frac{E_i}{kT_{\text{ex}}}. \quad (4)$$

Here, N_i , g_i , and E_i are the column density, degeneracy, and the energy of the upper level, respectively. A_{ij} is the Einstein coefficient of the transition. Q is the partition function, which depends on the excitation temperature T_{ex} .

The observed emission is attenuated by foreground material, necessitating additional care before the analysis. While the SED fitting result of [M. M. Dunham et al. \(2015\)](#) estimates a visual extinction of $A_V=9.6$ mag, we treat A_V as a free parameter in the excitation diagram fitting. We adopt the KP5 extinction curve, which is representative of icy dust in dense molecular clouds ([K. M. Pontoppidan et al. 2024](#)). For the KP5 extinction curve, the optical depth at the wavelength of H₂ S(3) line is calculated as $\tau_{9.7} = 0.1509A_V$. The impact of using different extinction curves is discussed in [Appendix E.2](#). The relation between the intrinsic intensity and the observed intensity is given by:

$$I_{\text{obs}} = 10^{-0.4A_\lambda} I_\nu = 10^{-0.4A_V(A_\lambda/A_V)} I_\nu. \quad (5)$$

Since the angular resolution and pixel scale vary with wavelength, we convolve all the line maps to match the size of the PSF of the transition with the longest wavelength. Although the PSF is not strictly Gaussian, we assume the observed images as convolutions of the true emission with a Gaussian kernel with FWHM from [Eq. 1](#). To match the PSF of the image from the shorter wavelength λ to the PSF of representative wavelength λ_0 , we

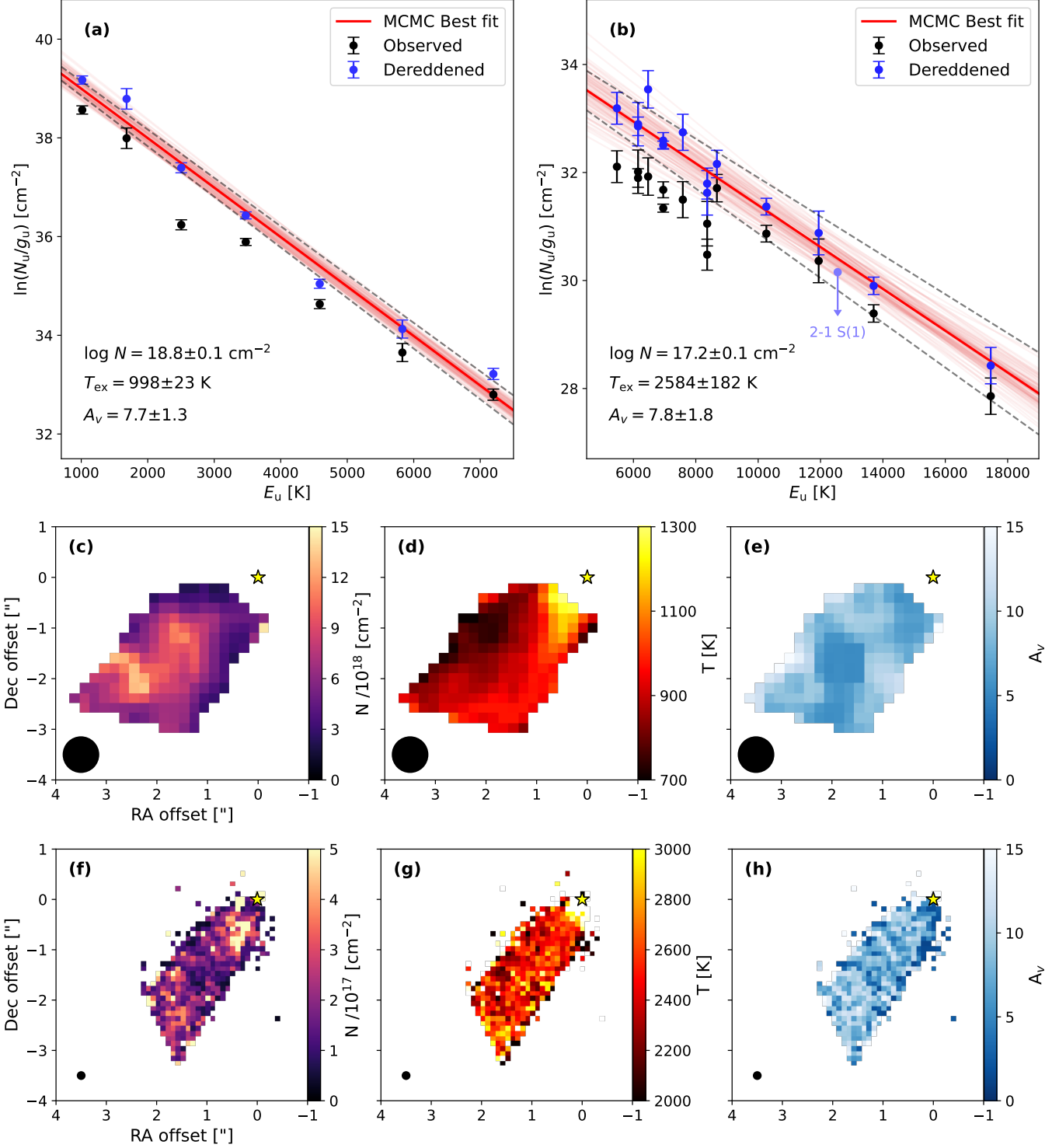


Figure 9. (a) MIRI H₂ excitation diagram result from a representative position of the outflow. The observed transitions are marked with black points, and blue points represent the measurements after extinction correction. The red line is the best-fit model, and the fainter lines are the posterior samples. Gray dashed lines indicate the models corresponding to the 16th and 84th percentiles. (b) Same with (a), but for NIRSpec transitions. The 3 σ limit for the undetected 2-1 S(1) transition is marked in lighter blue. (c, d, e) 2D distributions of H₂ column density, temperature, and extinction from the MIRI excitation diagram analysis. The position of the central source is marked with a yellow star. The black circle indicates the size of the convolved PSF. (f, g, h) Same as the row above, but for NIRSpec.

apply a Gaussian convolution to the shorter wavelength map with a FWHM calculated as follows:

$$\text{FWHM} = \sqrt{\theta_{\lambda_0}^2 - \theta_{\lambda}^2}. \quad (6)$$

Finally, all line maps are re-gridded to match the spatial grid of the transition with the longest wavelength. This procedure enables pixel-to-pixel analysis of excitation diagrams and yields spatially resolved maps of excitation temperature, column density, and extinction. The transitions within MIRI wavelengths and NIRSpec wavelengths are analyzed separately, since the spatial resolution of NIRSpec is much better, and there is a large flux discrepancy between the two instruments. The PSF FWHM and pixel size are $0.7''$ and $0.3''$ for MIRI wavelengths respectively, and $0.15''$ and $0.1''$ for NIRSpec, respectively.

For each pixel, we used the Markov-Chain Monte Carlo (MCMC) method to simultaneously fit the excitation temperature, column density, and extinction, along with their uncertainties. For detailed information about the MCMC fitting, refer to Appendix E.1.

The top panels of Figure 9 show examples for the excitation diagram. The black points from the original data-cubes do not align well along a straight line. However, after correcting for extinction, each excitation diagram is well explained with a single line.

Panels (c) - (e) show the results of the excitation diagram using MIRI wavelengths. The analysis was performed only on pixels where more than 4 H₂ lines were detected with S/N>3. The median column density of H₂, excitation temperature, and extinction are $6.4 \times 10^{18} \text{ cm}^{-2}$, 900 K, and 8.3, respectively. The H₂ outflow has a roughly constant temperature between 700–1000 K, except near the outflow base, where the temperature is significantly higher, exceeding 1200 K.

Panels (f) - (h) show similar maps, but for NIRSpec wavelengths. The emission region appears narrower than in the MIRI excitation maps, but this is partially due to the PSF being much smaller ($0.15''$) than that of MIRI ($0.7''$). The median column density of H₂, excitation temperature, and extinction are $1.8 \times 10^{17} \text{ cm}^{-2}$, 2500 K, and 8.1, respectively. Assuming the ro-vibrational transitions are in LTE and that this excitation diagram correctly reflects the gas kinetic temperature, the NIRSpec lines trace a hotter component than the MIRI lines. The column density of the hotter component is ~ 35 times less than the cooler component, so the cooler component represents the bulk of the outflowing material. The extinctions derived from both analyses agree well.

The 2–1 S(1) transition at $2.2477 \mu\text{m}$ is not detected above the 3σ level in any pixel. This line is often used

as a diagnostic of UV excitation or strong J-type shocks, since these mechanisms are expected to increase the 2–1/1–0 intensity ratio (K. F. Kaplan et al. 2021; L. E. Kristensen et al. 2023). Figure 9(b) shows the 3σ upper limit of the observed 2–1 S(1) line. This upper limit is consistent with the excitation diagram prediction, supporting a scenario in which the H₂ emission is predominantly thermally excited. If significant UV fluorescence or strong J-type shocks were present, the 2–1 S(1) flux would be expected to exceed the excitation-diagram prediction. No such excess is observed.

4.3. [Fe II] Jet Morphology

We analyzed the [Fe II] $5.34 \mu\text{m}$ emission line to determine the position angle (PA), opening angle, and launching radius of the atomic jet. For each horizontal row of pixels in the integrated intensity map, we measured the peak emission position and its width. A linear fit to the ALMA continuum center was used to determine the jet axis. The estimated PA is $142.2 \pm 0.4^\circ$. This is consistent with the PA of the Serpens filament (139°) and the typical PA of the outflows found in Serpens Main ($136 \pm 25^\circ$; J. D. Green et al. 2024). We estimate the jet’s opening angle and launching radius, following the method described in M. Narang et al. (2024). We first extracted transverse slices perpendicular to the jet axis, with a width along the jet equal to the empirical FWHM of the MIRI-MRS PSF at this wavelength ($\sim 0.28''$). Each slice was further divided into 21 narrower pixel-width smaller apertures ($0.13''$). We extracted the spectrum from each aperture and measured the integrated line flux. The jet width in each slice was then determined by fitting a Gaussian profile to the transverse flux distribution. A linear fit to the measured jet widths as a function of distance from the source yielded the jet opening angle (θ) and the base width ($R(0)$).

The middle panel of Figure 10 shows the apparent jet width increasing with distance from the central source. However, the observed jet width is broadened by the instrumental PSF, so we deconvolve the measured widths using Equation 2. Assuming a distance of 436 pc to EC 53 (G. N. Ortiz-León et al. 2017) and a disk inclination angle of 32° derived at Section 3.1, we calculated the intrinsic jet width and deprojected distance from the source for each slice. Finally, we derived the jet width at the base (half of the y-intercept) and the opening angle (using the slope) by using a linear fit; our linear fit to the deconvolved widths resulted in a base jet width (half of the y-intercept) of $49.9 \pm 2.4 \text{ au}$ and an opening angle of $1.29 \pm 0.11^\circ$. Alternatively, a parabolic fit yields a base width of $45.9 \pm 3.5 \text{ au}$, which we adopt as an upper limit on the jet-launching radius.

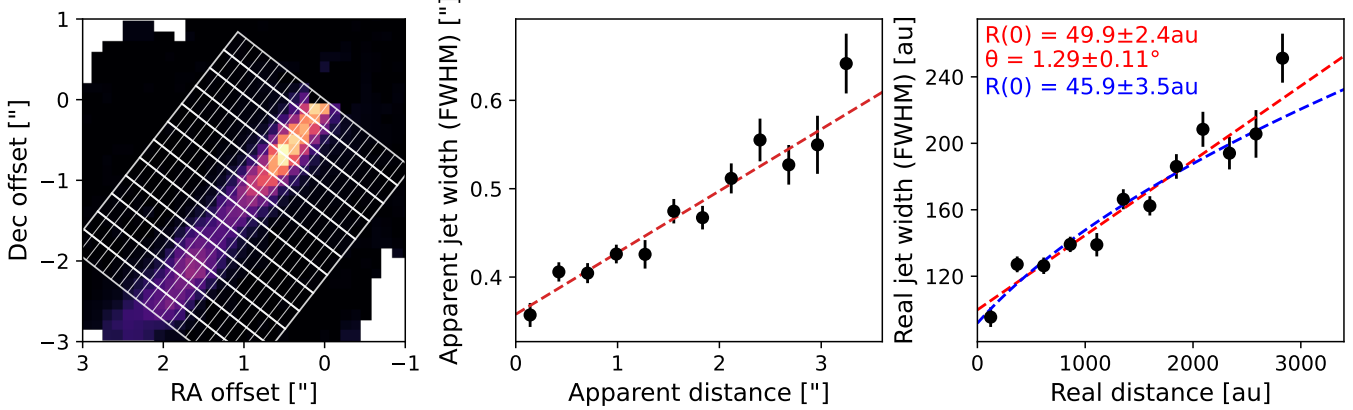


Figure 10. (Left) Apertures used for jet morphology analysis (white rectangles) overlaid on the [Fe II] 5.34 μm peak intensity map. (Middle) Apparent FWHM of the jet as a function of distance from the central source, shown in angular units. A red dashed line indicates the best-fit linear function. (Right) Deconvolved, real FWHM of the jet as a function of distance from the central source, shown in distance units. The red- and blue-dashed lines indicate the best-fit linear function and the best-fit parabolic function, respectively. Fit parameters are written in the corresponding colors.

The launching radius derived from our analysis (45.9 au) is comparable to values reported for other low-mass protostars, such as IRAS 16253-2429 (23 au; M. Narang et al. 2024), IRAS 15398-3359 (20.2 au), or B335 (37.1 au; S. A. Federman et al. 2024). However, these estimated jet launching radii are greater than the ones typically inferred from kinematic studies using SiO or optical tracers, which often yield values below 10 au (C.-F. Lee 2020). In the case of EC 53, the ALMA data do not reveal a collimated, jet-like high-velocity CO component, which limits our ability to directly constrain the jet size and its launching radius from CO kinematics alone. Moreover, it is important to note that the geometrically derived launching radius generally exceeds the MHD wind launching radius obtained through angular momentum measurements (I. Pascucci et al. 2023) and should, therefore, be considered only as an upper limit.

4.4. Outflow Velocity Distribution

We made velocity maps of strong emission lines to investigate the velocity distribution in the outflow. Using the continuum-subtracted data cubes, we fitted a Gaussian profile to each spaxel to derive the line-of-sight velocity at each position. The left panels of Figure 11 show the velocity maps for selected strong lines. In the H₂ lines, we observe the blueshifted outflow, with velocity increasing along the outflow axis away from the central source. The [Fe II] and [Ne II] lines trace the jet. The blueshifted jet is detected in all transitions, but only in the [Fe II] line at 26 μm , we detect the bipolar jet from both sides of the central source. The northwest lobe is red-shifted, while the southeast lobe is blue-shifted.

The right panel of Figure 11 shows the change in velocity along the jet axis. Following a similar method to our jet width analysis, we placed rectangular apertures 0.3" long perpendicular to the jet axis and calculated the average velocity within each aperture. The H₂ transitions can be categorized into two groups. Lower excitation lines ($E_u < 5000 \text{ K}$), with wavelengths longer than 6.5 μm maintain a relatively constant velocity of approximately 25 km s^{-1} along the jet axis. On the other hand, higher excitation lines exhibit significantly higher velocities, ranging between 40 and 60 km s^{-1} . Within this group, lines with higher excitation energy have higher velocities. Furthermore, these lines show a linear increase in velocity with distance from the source. Assuming the inclination of the H₂ outflow is the same as that of the jet (32°), the mean total velocity of each group is $\sim 30 \text{ km s}^{-1}$ and $\sim 60 \text{ km s}^{-1}$, respectively.

In contrast, the jet emission extends farther, and its velocity plateaus at $\sim 110 \text{ km s}^{-1}$ beyond 2" from the center for both lobes. There is some wiggling, which can be either from observation uncertainty or precession of the jet (C.-F. Lee 2020). The velocities of various jet lines are consistent with each other within 25 km s^{-1} . After correcting for the inclination, the terminal velocity of the jet is estimated to be $\sim 130 \text{ km s}^{-1}$. Notably, the zero-velocity position of the [Fe II] 25.99 μm line is offset by $\sim 1.5''$ into the redshifted lobe, which is a large discrepancy that cannot be explained solely by projection effects. The origin of this discrepancy is discussed further in Section 5.2.

4.5. Analysis of the mid-IR CO Emission

The CO spectra, which are mixed with emission and absorption features detected inside the outflow cavity,

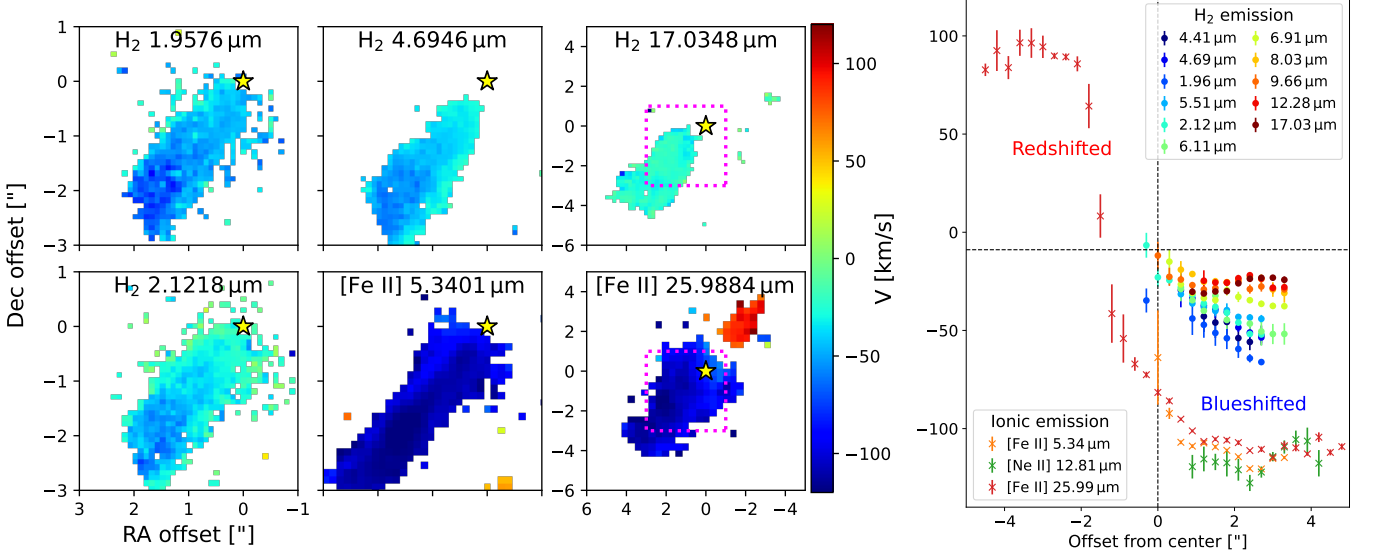


Figure 11. Velocity maps of selected lines (left). Note that the image size of the $17.03\,\mu\text{m}$ H₂ map and $25.99\,\mu\text{m}$ [Fe II] map is larger than the other maps of short wavelength transitions. The extent of the smaller maps is indicated by pink-dotted squares. Mean radial velocity curves of various emission lines along the jet (right). Positive offset is in the southeast direction, where the blueshifted outflow is located. Colors of the H₂ emission markers denote the upper energy levels of the transitions, with a gradient from red to blue representing increasing upper energy levels.

are likely produced by two distinct steps. First, CO molecules near the central protostar produce absorption lines against the continuum, primarily originating from the heated disk midplane (Seokho Lee et al. submitted). This is observed in the spectra extracted toward the central protostar (blue spectrum of Figure 5). Photons generated at the central source, including those with absorption features, are scattered along the line of sight through the outflow cavity, where hot CO gas is present. This CO gas is shock-heated by the outflow, producing emission lines. These emission lines are superimposed on the scattered continuum from the central source along our line of sight. If the emission lines are sufficiently strong, they can partially or fully fill in the absorption features seen in the scattered light. As a result, some CO lines appear in emission while others remain in absorption, as shown in the red spectrum of Figure 5. Finally, all radiation is further attenuated by dust and ice in the surrounding protostellar envelope. Multiple components of CO with different temperatures and origins have been reported in various young stellar objects (G. J. Herczeg et al. 2011), supporting this scenario.

Therefore, to study the emission distribution of the hot CO in the outflow, we extract the pure CO emission spectra following the process presented in Figure 12. The intensities that we observe from the center (I'_0) and the CO emission region (I'_1) can be expressed as

follows:

$$I'_0 = I_0 e^{-\tau_0}, \quad (7)$$

$$I'_1 = I_1 e^{-\tau_1} = (C I_0 + I_{CO}) e^{-\tau_1}. \quad (8)$$

I'_0 and I'_1 are the observed intensities obtained directly from the data (first panel of Figure 12). I_0 represents the intrinsic intensity at the central position, including the CO absorption lines. I_0 is attenuated by the envelope optical depth τ_0 before getting observed as I'_0 . In regions affected by the outflow, I_0 is reduced by a factor of C due to scattering. On the other hand, the hot CO gas shocked by the outflow adds the emission, I_{CO} , to the scattered emission, $C I_0$, making the total intensity, I_1 . This total intensity is attenuated by the envelope optical depth (τ_1) along the line of sight. However, the I'_1/I'_0 baseline, as presented with the red line in the second panel of Figure 12, is independent of line emission and only contains information about scattering effects and foreground attenuation ($C e^{\tau_0 - \tau_1}$). The baseline was obtained using the ‘mixture model’ method from the `pybaseline` Python package (D. Erb 2024). The mixture model treats each data point as arising from a probabilistic combination of a baseline and a signal distribution, allowing robust separation of a smooth baseline from sharp spectral features by reducing the influence of outliers (B. Ghojogh et al. 2019). The third panel compares the light from the outflow and the central flux multiplied by the baseline.

The final panel shows the residual after subtracting the two spectra ($I_{CO} e^{-\tau_1}$). The final residual shows all

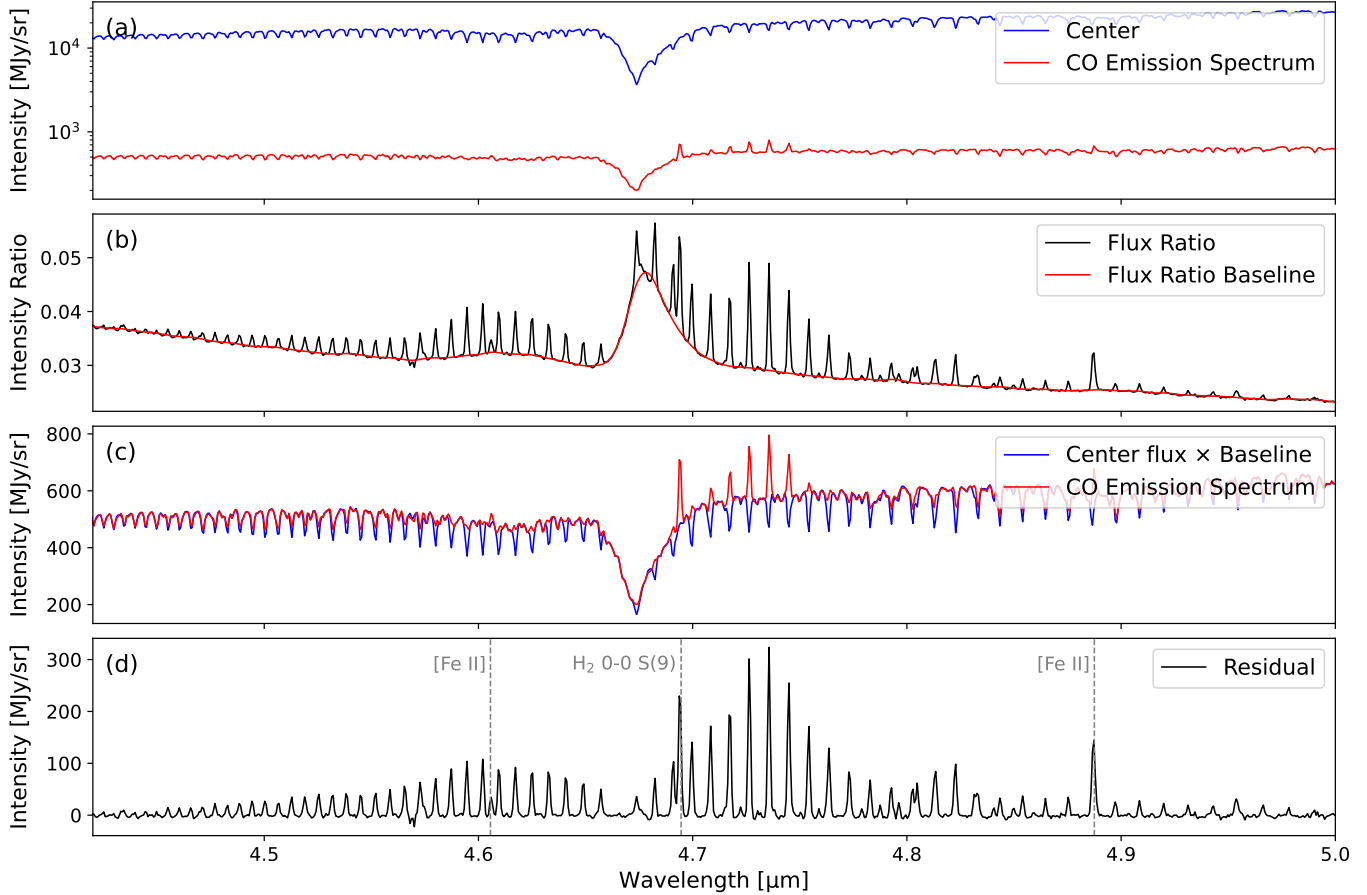


Figure 12. Derivation process of the hot CO emission. (a) Spectra extracted from the ALMA continuum center (blue) and a position with strong CO emission (red). (b) The ratio of the two spectra (black), with the fitted baseline (red), accounting for scattering and differences in foreground attenuation. (c) The central spectrum multiplied by the baseline (blue), compared with the observed CO emission spectrum (red). (d) The residual spectrum representing the hot CO component. Gray dashed lines mark the emission lines from other than CO.

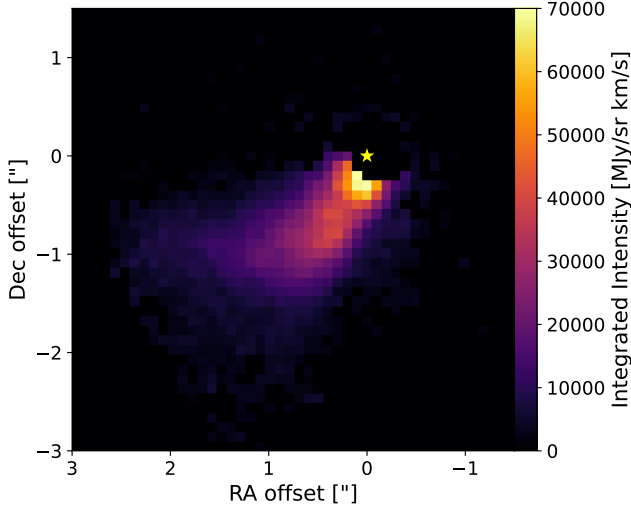


Figure 13. The residual integrated intensity map of CO v=1-0 P(8), after subtracting the scattered light, which includes the CO absorption spectra.

CO lines in emission, with the P-branch stronger than the R-branch. Although the foreground attenuation ($e^{-\tau_1}$) is not fully corrected, the attenuation is fairly constant in the wavelength range except for the CO ice absorption, and would not change the existence of the observed asymmetry between the P- and R-branch.

The procedure above can be applied to all pixels, including regions with no evident CO emission. Figure 13 shows the peak flux map of CO v=1-0 P(8) after subtracting the scattered continuum component, which includes the CO absorption features produced in the protostellar disk. Even in areas that originally showed CO absorption, the residual image shows emission if the absorption depth was less than that of the reference spectrum. The pixels near the center are masked because the absorption lines are stronger than those in the reference spectrum used for modeling the disk CO component. The spatial distribution of the residual emission resembles the H₂ emission, which traces hot gas in the outflow

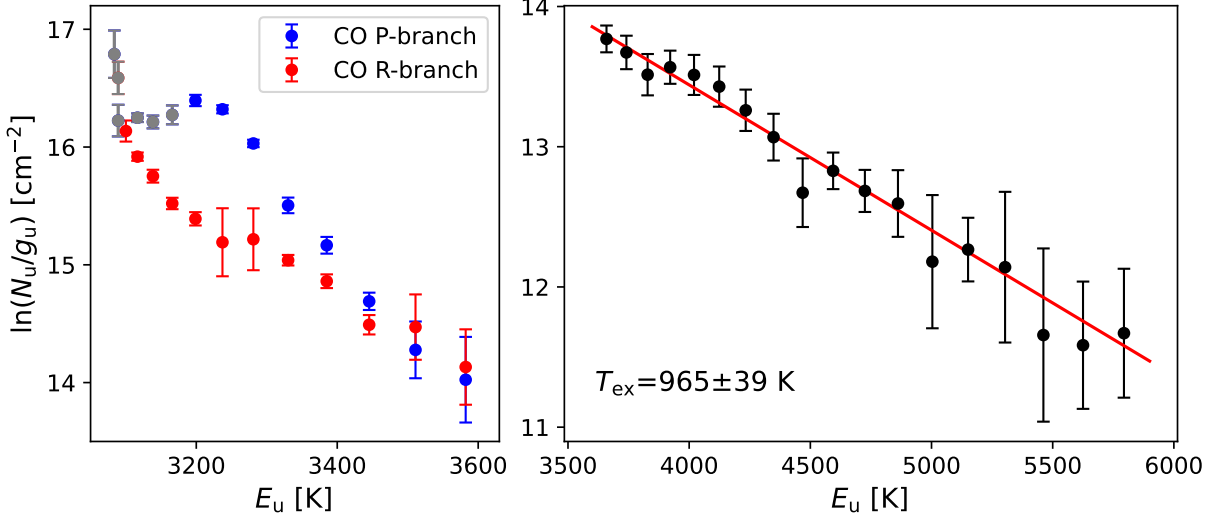


Figure 14. (Left) Excitation diagram of CO with low- J transitions. P-branch and R-branch transitions are marked in blue and red, respectively. Transitions contaminated by CO ice absorption are marked in gray. (Right) Excitation diagram of CO with high- J R-branch transitions.

cavity. This suggests that the hot CO and H₂ may share a common origin.

4.6. Excitation diagram of mid-IR CO

We utilized an excitation diagram to estimate the physical properties of the CO gas. The analysis was done using the residual emission shown in the last panel of Figure 12. Although the spectrum shows strong peaks of the ¹²CO $v=1-0$ lines, some transitions are heavily contaminated by CO ice absorption, H₂ emission, and ¹³CO emission.

Figure 14 shows the results. The low- J lines ($J < 11$) clearly exhibit the P-R asymmetry. P-R asymmetry has been observed in many astronomical environments, from protostars (E. González-Alfonso et al. 1998, 2002; A. E. Rubinstein et al. 2024) to AGN jets (V. A. Buitén et al. 2024; M. Pereira-Santalla et al. 2024). vibrationally excited CO molecules have very high critical densities ($\sim 10^{14}$ cm $^{-3}$ at $T \sim 1000$ K), which are much higher than typical gas densities in outflow cavities ($10^5 \sim 10^6$ cm $^{-3}$). In such low-density conditions, CO can deviate from LTE and become radiatively excited. In these cases, the P-branch emission can be stronger than the R-branch (E. González-Alfonso et al. 2002; J. H. Lacy 2013).

The right panel shows the excitation diagram using the high- J R-branch transitions. Only the R-branch transitions were used, as the P-branch transitions were more contaminated. The observed intensities could be explained by a single-component model with an excitation temperature of 965 K. The obtained excitation temperature of CO is similar to the excitation temperature

of purely rotational H₂ lines. However, this temperature may not reflect the kinetic temperature of CO, as the LTE assumption is invalid. The $v = 1$ levels of CO are primarily radiatively excited, and the excitation temperature is heavily influenced by the Planck temperature of the local radiation field (V. A. Buitén et al. 2024). Reliable non-LTE modeling requires collision coefficients for vibrationally excited CO with H₂. While some studies have modeled the emission using coefficients estimated from scaling relations (e.g., W. F. Thi et al. 2013; A. D. Bosman et al. 2019), accurate coefficients derived from quantum calculations are currently unavailable. Such modeling is beyond the scope of this paper and is left for future work.

4.7. Transverse Position-Velocity Diagram of ALMA CO Emission

As shown in Figure 15, the submillimeter CO emission traces both blueshifted and redshifted outflows, although large-scale emission suffers from the resolve-out effect due to the small maximum recoverable size (MRS $\sim 1.63''$) of our ALMA observation. Nevertheless, the redshifted CO emission is well detected close to the central protostar, allowing the small-scale redshifted outflow emission to be used for kinematic analysis. For this, we made transverse position-velocity (PV) diagrams across the outflow axis with a 0.15'' interval, as presented in the right panels of Figure 15. The transverse PV diagrams consist of 2 components: a narrow high-velocity feature and a wide low-velocity feature. The low-velocity feature has a trapezoidal shape, with

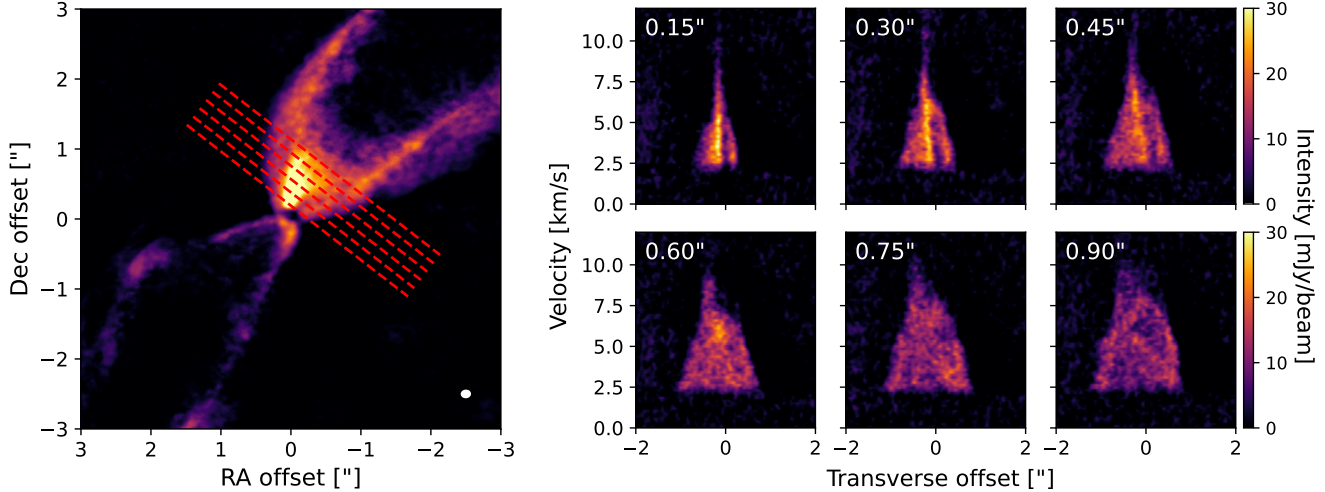


Figure 15. (Left) Integrated intensity map of the high-resolution ALMA CO observation. Red dashed lines denote the transverse PV cuts at intervals of $0.15''$. (Right) Transverse PV diagrams for each PV cut.

higher velocities near the jet axis and lower velocities on the edge.

5. DISCUSSION

5.1. Morphology and Possible Launching Mechanisms of the Outflow and Jet

Figure 16 presents the morphology of various outflow components of EC 53, observed with JWST and ALMA. The structure reveals an onion-like stratification within the wide outflow cavity traced by the short-wavelength NIRSpec continuum. Nested within this cavity are the cold CO outflow traced by ALMA, the hot H₂ emission, and the fast atomic jet. These components span a range of temperatures and velocities: the atomic jet traced with [Fe II] is well collimated and fast ($\sim 130 \text{ km s}^{-1}$), the hot H₂ component shows intermediate velocities and temperatures, while the cold CO outflow is slower ($< 10 \text{ km s}^{-1}$).

This layered structure with hotter, faster components enclosed within the cooler, slower ones is commonly seen in protostellar systems at various evolutionary stages (A. Caratti o Garatti et al. 2024; V. Delabrosse et al. 2024; S. A. Federman et al. 2024; L. Tychoniec et al. 2024; I. Pascucci et al. 2025). The onion-like layered structure is often interpreted as a defining characteristic of magneto-centrifugal disk winds (MHD winds), which naturally produce stratified outflows (R. D. Blandford & D. G. Payne 1982; J. Ferreira et al. 2006). In these models, hotter, faster material is launched from smaller radii in the disk, resulting in narrower opening angles and higher outflow velocities because of the higher Keplerian speeds at the base. The observed hierarchy in temperature and velocity among [Fe II], H₂, and cold CO in EC 53 supports this scenario.

Additionally, we find that this stratification persists within the H₂ gas itself, which shows a clear gradient in spatial extent, temperature, and velocity. The lower excitation transitions exhibit wider profiles ($\sim 1.7''$) that systematically narrow to a more collimated width ($\sim 1.1''$) at higher excitation. A similar trend is seen in temperature: transitions observed with MIRI yield excitation temperatures of $\sim 900 \text{ K}$, while higher-energy lines observed with NIRSpec trace significantly hotter gas at $\sim 2500 \text{ K}$. The lower-energy transitions show slower, relatively constant velocities of $\sim 30 \text{ km s}^{-1}$ along the jet axis, whereas higher-excitation transitions reach average velocities of $\sim 60 \text{ km s}^{-1}$.

Even within the cold CO emission, the PV diagram shows an inner, faster component nested within a slower one, consistent with predictions of MHD wind models (see Figure 15; A. de Valon et al. 2020).

One way to further test the MHD disk wind scenario is to measure the angular momentum and compute the magnetic lever arm parameter, λ . The magnetic lever arm parameter is the ratio of the outflow's specific angular momentum to the Keplerian value at the launching radius. In MHD winds, $\lambda > 1.5$, indicating efficient angular momentum removal from the disk. However, the spectral resolution of JWST spectra is insufficient to detect the small velocity gradients that would be expected from rotation in H₂ or [Fe II].

Another notable feature in EC 53 is the increase in H₂ velocity along the outflow axis, observed for higher energy transitions. This apparent acceleration could also arise from entrained envelope material rather than direct wind launching. Swept-up gas acceleration has been observed in several sources, including HH 211 (C.-F. Lee et al. 2022), Cep E (A. de A. Schutze et al. 2022), HOPS

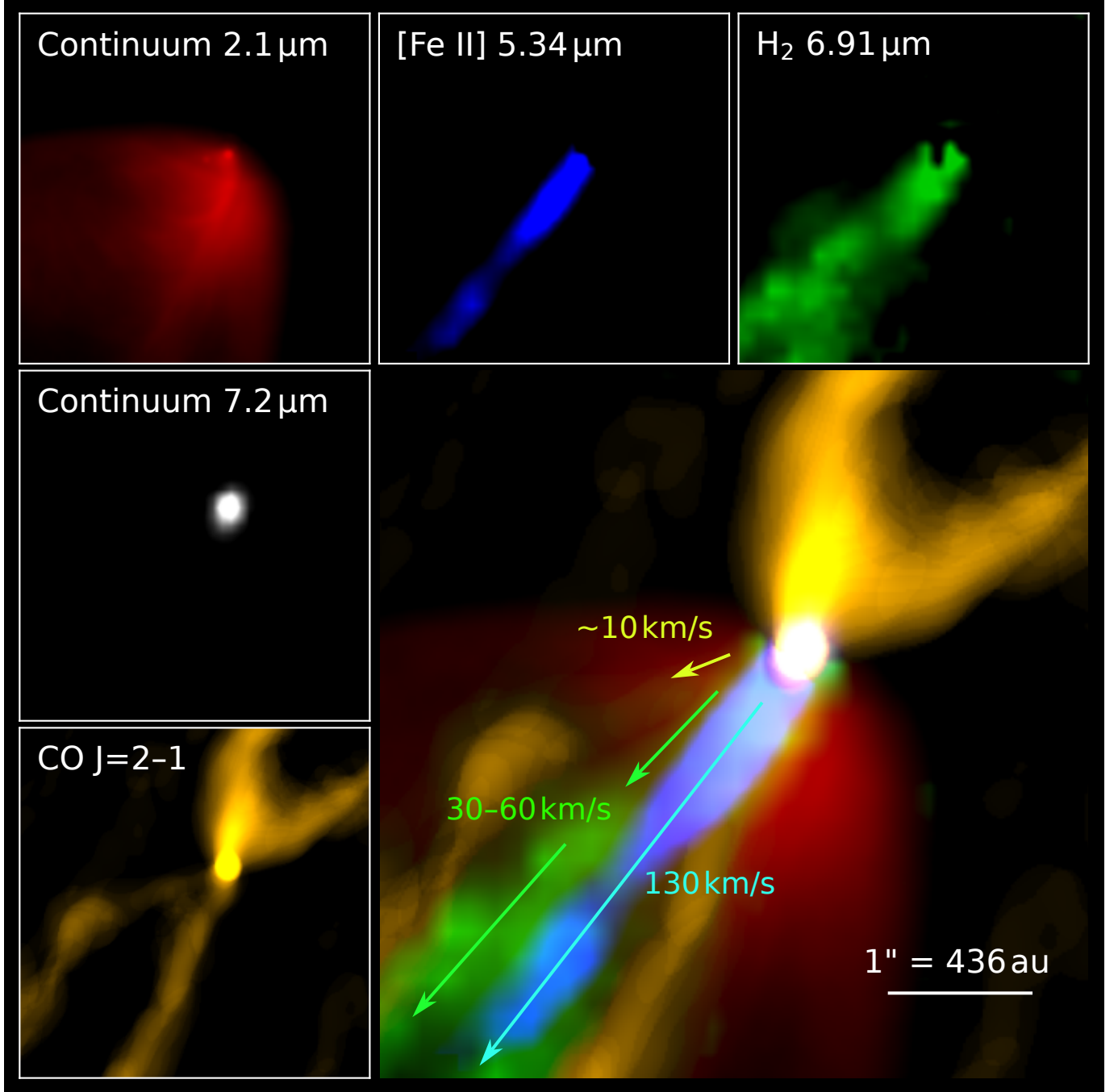


Figure 16. Images of different components of EC 53 (top and left) and their composite image (lower right). The color scale for each image is adjusted to best present its structure. The velocities of each component are marked with the same colors.

373SW (S. Lee et al. 2024), and HOPS 315 (C. Vleugels et al. 2025). The wide-angle wind-driven shell model (Z.-Y. Li & F. H. Shu 1996; C.-F. Lee et al. 2000) offers a plausible explanation: when a radial wind interacts with a flattened envelope, it drives a forward shock that sweeps up envelope material. This produces a radially expanding shell with velocity increasing linearly with distance from the source—a “Hubble-law”-like acceleration profile. However, the fact that this acceleration

is primarily seen in the narrower, higher energy lines suggests it may represent the acceleration of the inner wind entrained by the jet (M. D. Smith et al. 1997; M. Rabenahary et al. 2022). The constant velocity of the lower-excitation H₂ may represent a more stable, outer component of the disk wind that has experienced less interaction with the high-speed central jet.

In summary, while the observed stratification and acceleration patterns in EC 53 are broadly consistent with

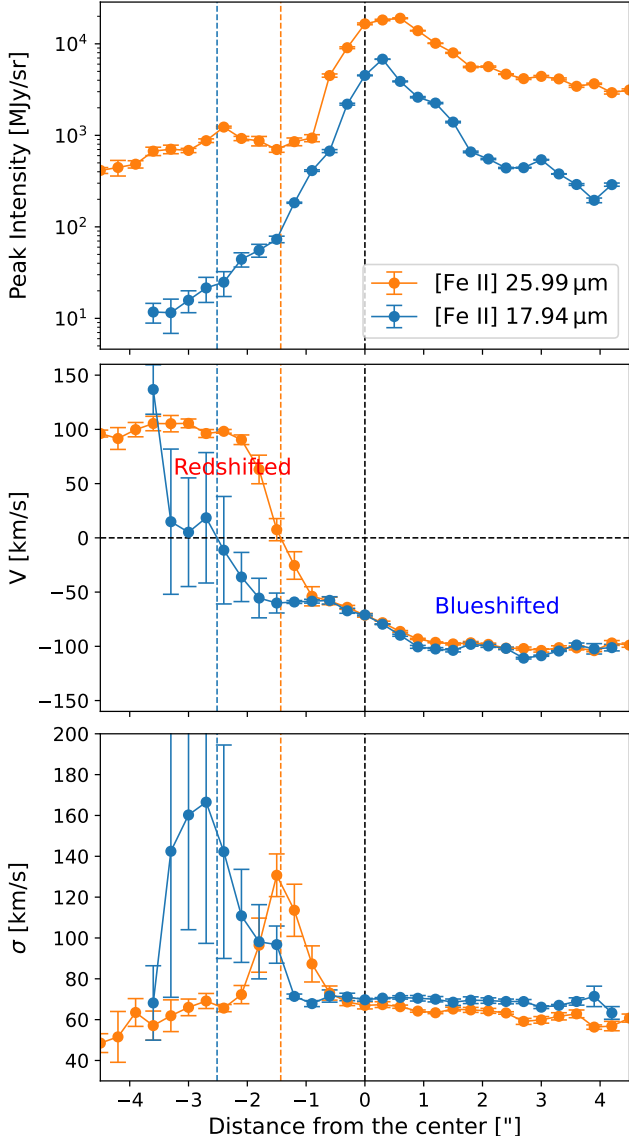


Figure 17. Peak intensity (top), Mean radial velocity (middle), and line width (bottom) of [Fe II] $25.99\text{ }\mu\text{m}$ (orange) and $17.94\text{ }\mu\text{m}$ (blue) line along the jet of EC 53. Positive offset is in the southeast direction, where the blueshifted jet is located. The velocities are corrected with the barycentric velocity of -8.9 km s^{-1} , but not with the inclination. Vertical dashed lines indicate the zero-velocity positions for each line.

MHD disk wind models, additional mechanisms, such as wide-angle winds or jet-driven entrainment, may also contribute. A full understanding should also explain the apparent separation between the dense, cold CO shell observed with ALMA and the broader outflow cavity traced by scattered continuum and C₂H. Higher spectral resolution and complementary observations will be necessary to disentangle these contributions and confirm the launching, confining, and entrainment mechanisms.

5.2. Interpretation of the Jet Velocity Offset

Jets launched from a protostar at an inclined angle are expected to have shifted velocity in their lobes separated by the central protostar. However, the velocity maps in Figure 11 reveal offsets between the zero-velocity position and the protostellar location. For instance, the transition from blueshift to redshift observed in the [Fe II] jet occurs approximately $1.5''$ northwest of the protostar, coinciding with the location of the redshifted submillimeter CO outflow.

To investigate this phenomenon, we compare two [Fe II] lines, as shown in Figure 17, which presents the peak intensities, radial velocities, and line widths of the $25.99\text{ }\mu\text{m}$ and $17.94\text{ }\mu\text{m}$ [Fe II] transitions. Both emission lines are detected on either side of the jet axis across the protostar. The blueshifted jet is brighter than the redshifted counterpart, with a stronger flux difference for the $17.94\text{ }\mu\text{m}$ line. In both cases, the zero-velocity position is offset to the northwest of the protostellar position. Notably, the offset of the $17.94\text{ }\mu\text{m}$ line ($\sim 2.5''$) is larger than that of the $25.99\text{ }\mu\text{m}$ line ($\sim 1.5''$). The line width also varies with position, reaching a maximum near the zero-velocity region.

This shift in the zero-velocity position of the [Fe II] lines may result from the effects of PSF and extinction. Near the central region, the redshifted and blueshifted jets overlap along the line of sight due to the relatively large PSF (FWHM of $0.70''$ for $17.94\text{ }\mu\text{m}$ and $0.96''$ for $25.99\text{ }\mu\text{m}$), leading to increased line broadening near the source. Moreover, compared to the blue-shifted emission, the red-shifted jet must traverse a thicker portion of the envelope, leading to stronger extinction. Consequently, the blended emission near the protostar appears blueshifted, shifting the apparent zero-velocity position toward the northwest. The larger offset observed in the $17.94\text{ }\mu\text{m}$ line can be explained by the greater extinction at shorter wavelengths. We therefore assert that the observed jet velocity offset is due primarily to optical depth and angular resolution issues and expect that the true velocity along the jet shifts quickly from around -130 km s^{-1} to 130 km s^{-1} across the source.

5.3. Effect of Variability on the Outflow

EC 53 is a protostar showing a quasi-periodic variability with a period of approximately 1.5 years, observed across wavelengths from near-IR to sub-mm (e.g., K. W. Hodapp 1999; K. W. Hodapp et al. 2012; Y.-H. Lee et al. 2020; L. Francis et al. 2022). The periodic brightening and fading are attributed to variable accretion (G. Baek et al. 2020), potentially triggered by interactions between the disk and a very close companion at a few AU separation (e.g., I. Bonnell & P. Bastien 1992; S.

Nayakshin & G. Lodato 2012). If each accretion burst led to an increased ejection activity, they could appear as knots in the jet. In our observation, we do not see any significant knot-like features. If there was a newly formed knot ejected every 1.5 years, using intrinsic jet velocity of 130 km s^{-1} and inclination of 32° , the apparent angular distance between the knots would be $0.033''$. This is 3 times smaller than the NIRSpec pixel scale ($0.1''$). Even if such a series of knots by periodic accretion existed, it would not be resolved with the spatial resolution of JWST.

6. SUMMARY

We observed the Class I protostar EC 53 with JWST NIRSpec/IFU and MIRI/MRS, in addition to ALMA, and compared the results with archival NIRCam and lower-resolution ALMA data to obtain a comprehensive view of its outflow and jet structure. The main findings are summarized below:

1. Scattered light from the outflow cavity is observed in NIRCam images (F140M, F210M, F360M, and F480M) and in the short-wavelength NIRSpec continuum. Only the southeast cavity, which faces the observer, is visible. At longer wavelengths ($>5 \mu\text{m}$), emission from the central source dominates. ALMA continuum data resolve a compact disk with a radius of $\sim 0.1''$.
2. A total of 27 H_2 emission lines are detected with NIRSpec and MIRI. The H_2 emission traces a narrow, cone-like structure within the outflow cavity. Using an excitation diagram, we derived the gas temperature, column density, and extinction. Lower energy transitions exhibit a warm temperature ($\sim 900 \text{ K}$), while the higher energy transitions trace a hotter component ($\sim 2500 \text{ K}$). Lower-excitation H_2 maintains a constant, slow velocity, while the highly excited gas accelerates linearly along the outflow axis and exhibits a higher mean velocity.
3. A high-velocity jet is detected in multiple metal forbidden lines ([Fe II], [Ni II], [Ne II]). These lines are predominantly blueshifted and dissect the H_2 emission region. Two lines ($17.94 \mu\text{m}$ and $25.99 \mu\text{m}$) also show redshifted emission. We derived a jet position angle of 142.2° , an opening angle of 1.3° , and an upper limit on the launching radius of 45.9 au . The intrinsic velocity of the jet is $\sim 130 \text{ km s}^{-1}$. The apparent zero-velocity position is offset to the redshifted side, likely due to extinction and PSF effects.

4. MIR CO ro-vibrational lines are primarily seen in absorption, but some P-branch lines appear in emission. This is attributed to hot CO gas in the outflow cavity, which emits above the central source's absorption spectrum. The isolated CO emission shows stronger P-branch emission than the R-branch, consistent with radiative excitation in low-density regions such as the outflow cavity.
5. Cold CO is detected with ALMA on both outflow lobes. A position-velocity (PV) diagram from high-resolution ALMA data shows that emission closer to the jet has a higher velocity. C_2H emission closely traces the outflow cavity walls.
6. The atomic jet, hot gas (H_2 , CO), and cold gas (CO) are spatially nested, consistent with predictions from MHD disk wind models. The acceleration of highly excited H_2 can also be explained by jet entrainment. The outflow-launching mechanism cannot be attributed to a single theory; multiple processes may act simultaneously.

Further detailed modeling and higher-spectral-resolution NIR spectroscopy will be essential to test and distinguish between these scenarios. Nevertheless, this study demonstrates the powerful synergy of ALMA and JWST in advancing our understanding of protostellar outflow and jet systems.

ACKNOWLEDGMENTS

This work was supported by the National Research Foundation of Korea (NRF) grant funded by the Korea government (MSIT) (grant numbers 2021R1A2C1011718 and RS-2024-00416859). D.J. is supported by NRC Canada and by an NSERC Discovery Grant. G.J.H. is supported by grant IS23020 from the Beijing Natural Science Foundation. J.D.G. acknowledges support from the associated 3477 NASA observer grant. This work is based on observations made with the NASA/ESA/CSA James Webb Space Telescope. The data were obtained from the Mikulski Archive for Space Telescopes at the Space Telescope Science Institute, which is operated by the Association of Universities for Research in Astronomy, Inc., under NASA contract NAS 5-03127 for JWST. These observations are associated with JWST program #3477 and #1611. This paper makes use of the following ALMA data: ADS/JAO.ALMA#2016.1.01304.T, ADS/JAO.ALMA#2019.1.01792.S, and ADS/JAO.ALMA#2022.1.00800.S. ALMA is a partnership

of ESO (representing its member states), NSF (USA), and NINS (Japan), together with NRC (Canada), MOST, and ASIAA (Taiwan), and KASI (Republic of Korea), in cooperation with the Republic of Chile. The Joint ALMA Observatory is operated by ESO, AUI/NRAO, and NAOJ. Some of the data presented in this article were obtained from the Mikulski Archive for Space Telescopes (MAST) at the Space Telescope Science Institute. The specific observations analyzed can be accessed via [doi:10.17909/h56s-xr27](https://doi.org/10.17909/h56s-xr27) and

[doi:10.17909/pv1h-ta47](https://doi.org/10.17909/pv1h-ta47). This research also uses data from the ALMA archive. We acknowledge the use of ChatGPT to check English grammar and improve the clarity of expressions.

Facilities : JWST, ALMA

Software : Numpy (C. R. Harris et al. 2020), Scipy (P. Virtanen et al. 2020), Astropy (Astropy Collaboration et al. 2022), Matplotlib (J. D. Hunter 2007), photutils (L. Bradley et al. 2016), emcee (D. Foreman-Mackey et al. 2013), corner (D. Foreman-Mackey 2016), pybase-lines (D. Erb 2024).

REFERENCES

Aikawa, Y., Kamuro, D., Sakon, I., et al. 2012, A&A, 538, A57, doi: [10.1051/0004-6361/201015999](https://doi.org/10.1051/0004-6361/201015999)

Arce, H. G., Shepherd, D., Gueth, F., et al. 2007, in Protostars and Planets V, ed. B. Reipurth, D. Jewitt, & K. Keil, 245, doi: [10.48550/arXiv.astro-ph/0603071](https://doi.org/10.48550/arXiv.astro-ph/0603071)

Assani, K. D., Harsono, D., Ramsey, J. P., et al. 2024, A&A, 688, A26, doi: [10.1051/0004-6361/202449745](https://doi.org/10.1051/0004-6361/202449745)

Assani, K. D., Li, Z.-Y., Ramsey, J. P., et al. 2025, A&A, 701, A175, doi: [10.1051/0004-6361/202555016](https://doi.org/10.1051/0004-6361/202555016)

Astropy Collaboration, Price-Whelan, A. M., Lim, P. L., et al. 2022, ApJ, 935, 167, doi: [10.3847/1538-4357/ac7c74](https://doi.org/10.3847/1538-4357/ac7c74)

Bachiller, R. 1996, ARA&A, 34, 111, doi: [10.1146/annurev.astro.34.1.111](https://doi.org/10.1146/annurev.astro.34.1.111)

Baek, G., MacFarlane, B. A., Lee, J.-E., et al. 2020, ApJ, 895, 27, doi: [10.3847/1538-4357/ab8ad4](https://doi.org/10.3847/1538-4357/ab8ad4)

Bai, X.-N., & Stone, J. M. 2013, ApJ, 769, 76, doi: [10.1088/0004-637X/769/1/76](https://doi.org/10.1088/0004-637X/769/1/76)

Balbus, S. A., & Hawley, J. F. 1991, ApJ, 376, 214, doi: [10.1086/170270](https://doi.org/10.1086/170270)

Bally, J. 2016, ARA&A, 54, 491, doi: [10.1146/annurev-astro-081915-023341](https://doi.org/10.1146/annurev-astro-081915-023341)

Blandford, R. D., & Payne, D. G. 1982, MNRAS, 199, 883, doi: [10.1093/mnras/199.4.883](https://doi.org/10.1093/mnras/199.4.883)

Bodenheimer, P. 1995, ARA&A, 33, 199, doi: [10.1146/annurev.aa.33.090195.001215](https://doi.org/10.1146/annurev.aa.33.090195.001215)

Bonnell, I., & Bastien, P. 1992, ApJL, 401, L31, doi: [10.1086/186663](https://doi.org/10.1086/186663)

Bosman, A. D., Banzatti, A., Bruderer, S., et al. 2019, A&A, 631, A133, doi: [10.1051/0004-6361/201935910](https://doi.org/10.1051/0004-6361/201935910)

Bradley, L., Sipocz, B., Robitaille, T., et al. 2016, in Astrophysics Source Code Library, record ascl:1609.011

Buitjen, V. A., van der Werf, P. P., Viti, S., et al. 2024, ApJ, 966, 166, doi: [10.3847/1538-4357/ad344b](https://doi.org/10.3847/1538-4357/ad344b)

Caratti o Garatti, A., Ray, T. P., Kavanagh, P. J., et al. 2024, A&A, 691, A134, doi: [10.1051/0004-6361/202451350](https://doi.org/10.1051/0004-6361/202451350)

Chapman, N. L., Mundy, L. G., Lai, S.-P., & Evans, II, N. J. 2009, ApJ, 690, 496, doi: [10.1088/0004-637X/690/1/496](https://doi.org/10.1088/0004-637X/690/1/496)

de A. Schutzer, A., Rivera-Ortiz, P. R., Lefloch, B., et al. 2022, A&A, 662, A104, doi: [10.1051/0004-6361/202142931](https://doi.org/10.1051/0004-6361/202142931)

de Valon, A., Dougados, C., Cabrit, S., et al. 2020, A&A, 634, L12, doi: [10.1051/0004-6361/201936950](https://doi.org/10.1051/0004-6361/201936950)

Delabrosse, V., Dougados, C., Cabrit, S., et al. 2024, A&A, 688, A173, doi: [10.1051/0004-6361/202449176](https://doi.org/10.1051/0004-6361/202449176)

D'Eugenio, F., Pérez-González, P. G., Maiolino, R., et al. 2024, Nature Astronomy, 8, 1443, doi: [10.1038/s41550-024-02345-1](https://doi.org/10.1038/s41550-024-02345-1)

Dunham, M. M., Allen, L. E., Evans, Neal J., I., et al. 2015, ApJS, 220, 11, doi: [10.1088/0067-0049/220/1/11](https://doi.org/10.1088/0067-0049/220/1/11)

Erb, D. 2024, v1.1.0 Zenodo, doi: [10.5281/zenodo.10676584](https://doi.org/10.5281/zenodo.10676584)

Ercolano, B., & Pascucci, I. 2017, Royal Society Open Science, 4, 170114, doi: [10.1098/rsos.170114](https://doi.org/10.1098/rsos.170114)

Federman, S. A., Megeath, S. T., Rubinstein, A. E., et al. 2024, ApJ, 966, 41, doi: [10.3847/1538-4357/ad2fa0](https://doi.org/10.3847/1538-4357/ad2fa0)

Ferreira, J., Dougados, C., & Cabrit, S. 2006, A&A, 453, 785, doi: [10.1051/0004-6361:20054231](https://doi.org/10.1051/0004-6361:20054231)

Foreman-Mackey, D. 2016, The Journal of Open Source Software, 1, 24, doi: [10.21105/joss.00024](https://doi.org/10.21105/joss.00024)

Foreman-Mackey, D., Hogg, D. W., Lang, D., & Goodman, J. 2013, PASP, 125, 306, doi: [10.1086/670067](https://doi.org/10.1086/670067)

Francis, L., Johnstone, D., Lee, J.-E., et al. 2022, ApJ, 937, 29, doi: [10.3847/1538-4357/ac8a9e](https://doi.org/10.3847/1538-4357/ac8a9e)

Frank, A., Ray, T. P., Cabrit, S., et al. 2014, in Protostars and Planets VI, ed. H. Beuther, R. S. Klessen, C. P. Dullemond, & T. Henning, 451, doi: [10.2458/azu_uapress_9780816531240-ch020](https://doi.org/10.2458/azu_uapress_9780816531240-ch020)

Fuente, A., Martin-Pintado, J., Cernicharo, J., & Bachiller, R. 1993, A&A, 276, 473

Ghojogh, B., Ghojogh, A., Crowley, M., & Karray, F. 2019, arXiv e-prints, arXiv:1901.06708, doi: [10.48550/arXiv.1901.06708](https://doi.org/10.48550/arXiv.1901.06708)

González-Alfonso, E., Cernicharo, J., van Dishoeck, E. F., Wright, C. M., & Heras, A. 1998, ApJL, 502, L169, doi: [10.1086/311503](https://doi.org/10.1086/311503)

González-Alfonso, E., Wright, C. M., Cernicharo, J., et al. 2002, A&A, 386, 1074, doi: [10.1051/0004-6361:20020362](https://doi.org/10.1051/0004-6361:20020362)

Gordon, I., Rothman, L., Hargreaves, R., et al. 2026, Journal of Quantitative Spectroscopy and Radiative Transfer, 109807, doi: <https://doi.org/10.1016/j.jqsrt.2026.109807>

Green, J. D., Pontoppidan, K. M., Reiter, M., et al. 2024, ApJ, 972, 5, doi: [10.3847/1538-4357/ad5a02](https://doi.org/10.3847/1538-4357/ad5a02)

Harris, C. R., Millman, K. J., van der Walt, S. J., et al. 2020, Nature, 585, 357, doi: [10.1038/s41586-020-2649-2](https://doi.org/10.1038/s41586-020-2649-2)

Harsono, D., Bjerkeli, P., Ramsey, J. P., et al. 2023, ApJL, 951, L32, doi: [10.3847/2041-8213/acdfca](https://doi.org/10.3847/2041-8213/acdfca)

Hensley, B. S., & Draine, B. T. 2021, ApJ, 906, 73, doi: [10.3847/1538-4357/abc8f1](https://doi.org/10.3847/1538-4357/abc8f1)

Herczeg, G. J., Brown, J. M., van Dishoeck, E. F., & Pontoppidan, K. M. 2011, A&A, 533, A112, doi: [10.1051/0004-6361/201016246](https://doi.org/10.1051/0004-6361/201016246)

Hirano, N., Ho, P. P. T., Liu, S.-Y., et al. 2010, ApJ, 717, 58, doi: [10.1088/0004-637X/717/1/58](https://doi.org/10.1088/0004-637X/717/1/58)

Hodapp, K. W. 1999, AJ, 118, 1338, doi: [10.1086/301003](https://doi.org/10.1086/301003)

Hodapp, K. W., Chini, R., Watermann, R., & Lemke, R. 2012, ApJ, 744, 56, doi: [10.1088/0004-637X/744/1/56](https://doi.org/10.1088/0004-637X/744/1/56)

Hsieh, C.-H., Arce, H. G., Maureira, M. J., et al. 2024, ApJ, 973, 138, doi: [10.3847/1538-4357/ad6152](https://doi.org/10.3847/1538-4357/ad6152)

Hunter, J. D. 2007, Computing in Science and Engineering, 9, 90, doi: [10.1109/MCSE.2007.55](https://doi.org/10.1109/MCSE.2007.55)

Jørgensen, J. K., Bourke, T. L., Myers, P. C., et al. 2007, ApJ, 659, 479, doi: [10.1086/512230](https://doi.org/10.1086/512230)

Kaplan, K. F., Dinerstein, H. L., Kim, H., & Jaffe, D. T. 2021, ApJ, 919, 27, doi: [10.3847/1538-4357/ac0899](https://doi.org/10.3847/1538-4357/ac0899)

Kramida, A., Ralchenko, Y., Reader, J., & Team, N. A. 2023, <https://physics.nist.gov/asd>

Kristensen, L. E., Godard, B., Guillard, P., Gusdorf, A., & Pineau des Forets, G. 2023, A&A, 675, A86, doi: [10.1051/0004-6361/202346254](https://doi.org/10.1051/0004-6361/202346254)

Lacy, J. H. 2013, ApJ, 765, 130, doi: [10.1088/0004-637X/765/2/130](https://doi.org/10.1088/0004-637X/765/2/130)

Law, D. R., E. Morrison, J., Argyriou, I., et al. 2023, AJ, 166, 45, doi: [10.3847/1538-3881/acdddc](https://doi.org/10.3847/1538-3881/acdddc)

Lee, C.-F. 2020, A&A Rv, 28, 1, doi: [10.1007/s00159-020-0123-7](https://doi.org/10.1007/s00159-020-0123-7)

Lee, C.-F., Ho, P. T. P., Li, Z.-Y., et al. 2017, Nature Astronomy, 1, 0152, doi: [10.1038/s41550-017-0152](https://doi.org/10.1038/s41550-017-0152)

Lee, C.-F., Li, Z.-Y., Shang, H., & Hirano, N. 2022, ApJL, 927, L27, doi: [10.3847/2041-8213/ac59c0](https://doi.org/10.3847/2041-8213/ac59c0)

Lee, C.-F., Mundy, L. G., Reipurth, B., Ostriker, E. C., & Stone, J. M. 2000, ApJ, 542, 925, doi: [10.1086/317056](https://doi.org/10.1086/317056)

Lee, C.-F., Li, Z.-Y., Codella, C., et al. 2018, ApJ, 856, 14, doi: [10.3847/1538-4357/aaaef6](https://doi.org/10.3847/1538-4357/aaaef6)

Lee, J.-E., Kim, C.-H., Kim, J., et al. 2026, Nature, 649, 853, doi: [10.1038/s41586-025-09939-3](https://doi.org/10.1038/s41586-025-09939-3)

Lee, S., Lee, J.-E., Aikawa, Y., Herczeg, G., & Johnstone, D. 2020, ApJ, 889, 20, doi: [10.3847/1538-4357/ab5a7e](https://doi.org/10.3847/1538-4357/ab5a7e)

Lee, S., Lee, J.-E., Johnstone, D., Herczeg, G. J., & Aikawa, Y. 2024, ApJ, 964, 34, doi: [10.3847/1538-4357/ad21e3](https://doi.org/10.3847/1538-4357/ad21e3)

Lee, Y.-H., Johnstone, D., Lee, J.-E., et al. 2020, ApJ, 903, 5, doi: [10.3847/1538-4357/abb6fe](https://doi.org/10.3847/1538-4357/abb6fe)

Lesur, G. R. J. 2021, A&A, 650, A35, doi: [10.1051/0004-6361/202040109](https://doi.org/10.1051/0004-6361/202040109)

Li, Z.-Y., & Shu, F. H. 1996, ApJ, 472, 211, doi: [10.1086/178056](https://doi.org/10.1086/178056)

Liang, L., Johnstone, D., Cabrit, S., & Kristensen, L. E. 2020, ApJ, 900, 15, doi: [10.3847/1538-4357/aba830](https://doi.org/10.3847/1538-4357/aba830)

López-Vázquez, J. A., Lee, C.-F., Shang, H., et al. 2024, ApJ, 977, 126, doi: [10.3847/1538-4357/ad8eb4](https://doi.org/10.3847/1538-4357/ad8eb4)

Matt, S., & Pudritz, R. E. 2005, ApJL, 632, L135, doi: [10.1086/498066](https://doi.org/10.1086/498066)

Matt, S., & Pudritz, R. E. 2008, ApJ, 678, 1109, doi: [10.1086/533428](https://doi.org/10.1086/533428)

McKee, C. F., & Ostriker, E. C. 2007, ARA&A, 45, 565, doi: [10.1146/annurev.astro.45.051806.110602](https://doi.org/10.1146/annurev.astro.45.051806.110602)

McMullin, J. P., Waters, B., Schiebel, D., Young, W., & Golap, K. 2007, in Astronomical Society of the Pacific Conference Series, Vol. 376, Astronomical Data Analysis Software and Systems XVI, ed. R. A. Shaw, F. Hill, & D. J. Bell, 127

Narang, M., Ohashi, N., Tobin, J. J., et al. 2025, AJ, 169, 192, doi: [10.3847/1538-3881/adb1ba](https://doi.org/10.3847/1538-3881/adb1ba)

Narang, M., Manoj, P., Tyagi, H., et al. 2024, ApJL, 962, L16, doi: [10.3847/2041-8213/ad1de3](https://doi.org/10.3847/2041-8213/ad1de3)

Navarro, M. G., Nisini, B., Giannini, T., et al. 2025, ApJ, 995, 199, doi: [10.3847/1538-4357/ae1f8f](https://doi.org/10.3847/1538-4357/ae1f8f)

Nayakshin, S., & Lodato, G. 2012, MNRAS, 426, 70, doi: [10.1111/j.1365-2966.2012.21612.x](https://doi.org/10.1111/j.1365-2966.2012.21612.x)

Nisini, B., Navarro, M. G., Giannini, T., et al. 2024, ApJ, 967, 168, doi: [10.3847/1538-4357/ad3d5a](https://doi.org/10.3847/1538-4357/ad3d5a)

Okoda, Y., Yang, Y.-L., Evans, II, N. J., et al. 2025, ApJ, 982, 149, doi: [10.3847/1538-4357/adb83f](https://doi.org/10.3847/1538-4357/adb83f)

Ortiz-León, G. N., Dzib, S. A., Kounkel, M. A., et al. 2017, ApJ, 834, 143, doi: [10.3847/1538-4357/834/2/143](https://doi.org/10.3847/1538-4357/834/2/143)

Pascucci, I., Cabrit, S., Edwards, S., et al. 2023, in Astronomical Society of the Pacific Conference Series, Vol. 534, Protostars and Planets VII, ed. S. Inutsuka, Y. Aikawa, T. Muto, K. Tomida, & M. Tamura, 567, doi: [10.48550/arXiv.2203.10068](https://doi.org/10.48550/arXiv.2203.10068)

Pascucci, I., Beck, T. L., Cabrit, S., et al. 2025, *Nature Astronomy*, 9, 81, doi: [10.1038/s41550-024-02385-7](https://doi.org/10.1038/s41550-024-02385-7)

Pereira-Santaella, M., González-Alfonso, E., García-Bernete, I., García-Burillo, S., & Rigopoulou, D. 2024, *A&A*, 681, A117, doi: [10.1051/0004-6361/202347942](https://doi.org/10.1051/0004-6361/202347942)

Pontoppidan, K. M., Evans, N., Bergner, J., & Yang, Y.-L. 2024, *Research Notes of the American Astronomical Society*, 8, 68, doi: [10.3847/2515-5172/ad303f](https://doi.org/10.3847/2515-5172/ad303f)

Pudritz, R. E., Ouyed, R., Fendt, C., & Brandenburg, A. 2007, in *Protostars and Planets V*, ed. B. Reipurth, D. Jewitt, & K. Keil, 277, doi: [10.48550/arXiv.astro-ph/0603592](https://doi.org/10.48550/arXiv.astro-ph/0603592)

Pudritz, R. E., & Ray, T. P. 2019, *Frontiers in Astronomy and Space Sciences*, 6, 54, doi: [10.3389/fspas.2019.00054](https://doi.org/10.3389/fspas.2019.00054)

Rabenahary, M., Cabrit, S., Meliani, Z., & Pineau des Forets, G. 2022, *A&A*, 664, A118, doi: [10.1051/0004-6361/202243139](https://doi.org/10.1051/0004-6361/202243139)

Ray, T. P., & Ferreira, J. 2021, *NewAR*, 93, 101615, doi: [10.1016/j.newar.2021.101615](https://doi.org/10.1016/j.newar.2021.101615)

Ray, T. P., McCaughrean, M. J., Caratti o Garatti, A., et al. 2023, *Nature*, 622, 48, doi: [10.1038/s41586-023-06551-1](https://doi.org/10.1038/s41586-023-06551-1)

Rubinstein, A. E., Evans, N. J., Tyagi, H., et al. 2024, *ApJ*, 974, 112, doi: [10.3847/1538-4357/ad6b92](https://doi.org/10.3847/1538-4357/ad6b92)

Shu, F., Najita, J., Ostriker, E., et al. 1994, *ApJ*, 429, 781, doi: [10.1086/174363](https://doi.org/10.1086/174363)

Shu, F. H., Adams, F. C., & Lizano, S. 1987, *ARA&A*, 25, 23, doi: [10.1146/annurev.aa.25.090187.000323](https://doi.org/10.1146/annurev.aa.25.090187.000323)

Smith, M. D., Suttner, G., & Yorke, H. W. 1997, *A&A*, 323, 223

Tafalla, M., Myers, P. C., Mardones, D., & Bachiller, R. 2000, *A&A*, 359, 967, doi: [10.48550/arXiv.astro-ph/0005525](https://doi.org/10.48550/arXiv.astro-ph/0005525)

Terebey, S., Shu, F. H., & Cassen, P. 1984, *ApJ*, 286, 529, doi: [10.1086/162628](https://doi.org/10.1086/162628)

Thi, W. F., Kamp, I., Woitke, P., et al. 2013, *A&A*, 551, A49, doi: [10.1051/0004-6361/201219210](https://doi.org/10.1051/0004-6361/201219210)

Tychoniec, L., van Dishoeck, E. F., van't Hoff, M. L. R., et al. 2021, *A&A*, 655, A65, doi: [10.1051/0004-6361/202140692](https://doi.org/10.1051/0004-6361/202140692)

Tychoniec, L., van Gelder, M. L., van Dishoeck, E. F., et al. 2024, *A&A*, 687, A36, doi: [10.1051/0004-6361/202348889](https://doi.org/10.1051/0004-6361/202348889)

van Dishoeck, E. F., Tychoniec, L., Rocha, W. R. M., et al. 2025, *A&A*, 699, A361, doi: [10.1051/0004-6361/202554444](https://doi.org/10.1051/0004-6361/202554444)

van Gelder, M. L., Ressler, M. E., van Dishoeck, E. F., et al. 2024, *A&A*, 682, A78, doi: [10.1051/0004-6361/202348118](https://doi.org/10.1051/0004-6361/202348118)

van Hoof, P. A. M. 2018, *Galaxies*, 6, 63, doi: [10.3390/galaxies6020063](https://doi.org/10.3390/galaxies6020063)

Virtanen, P., Gommers, R., Oliphant, T. E., et al. 2020, *Nature Methods*, 17, 261, doi: [10.1038/s41592-019-0686-2](https://doi.org/10.1038/s41592-019-0686-2)

Vleugels, C., McClure, M., Sturm, A., & Vlasblom, M. 2025, *A&A*, 695, A145, doi: [10.1051/0004-6361/202452475](https://doi.org/10.1051/0004-6361/202452475)

Yang, Y.-L., Green, J. D., Pontoppidan, K. M., et al. 2022, *ApJL*, 941, L13, doi: [10.3847/2041-8213/aca289](https://doi.org/10.3847/2041-8213/aca289)

APPENDIX

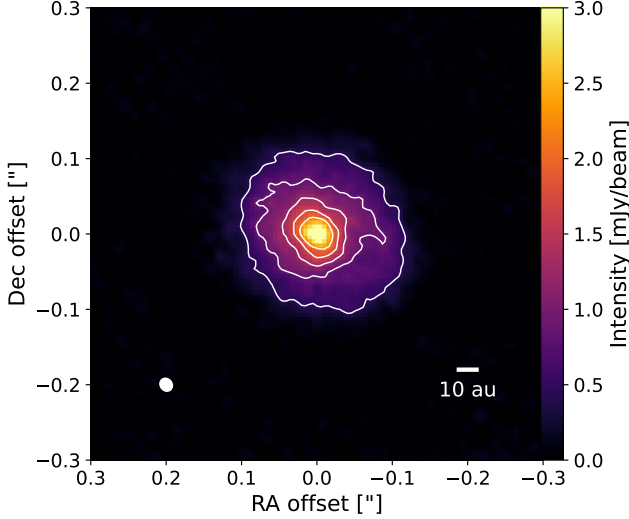


Figure A1. ALMA Continuum of EC 53. The contours are $10, 20, 30, 40, 50\sigma$ ($\sigma = 0.043 \text{ mJy beam}^{-1}$). The beam size is marked as a white ellipse.

A. ALMA CONTINUUM OF EC 53

In this section, the ALMA Band 7 continuum of EC 53 is presented in Figure A1. As explained in Section 3.1, the emission is from the protostar and the surrounding protoplanetary disk.

B. HOT/COLD PIXEL EXTRACTION

The original JWST Calibration Pipeline was insufficient for fully removing hot and cold pixels, particularly in NIRSpec data. Although most artifacts appeared near the image edges and did not affect the scientific analysis, a small number of hot and cold pixels were present within the outflow region. To address this, we implemented a two-step method to remove artifacts. First, we used the `detect_sources` function from the `photutils` Python package to identify and remove hot pixels. For each image slice, we detected sources with an intensity threshold of 90% of the image maximum. The largest detected source corresponds to the target itself, while the remaining detections were treated as artifacts. These artifacts were flagged and removed to produce the final science image. We used a median filter with size 5×5 to smooth out the flagged pixels. Second, for the hot-pixel-removed images, we computed the background intensity level only from the unflagged pixels. The cold pixels with brightness more than 3σ below the mean background were also flagged and median-filtered. Figure B2 illustrates this procedure.

This two-step method effectively removed a significant portion of the hot and cold pixels; however, it is not able to remove low-intensity artifacts. Lowering the detection threshold could enable us to remove such features, but it would increase the area identified as the central source. Consequently, any hot/cold pixels located close to the central source may be incorporated into the central footprint and falsely preserved rather than flagged as artifacts. To avoid this misidentification, we used conservative threshold values.

C. COMPARISON OF FLUX BETWEEN SPECTRAL BANDS

Figure C3 shows spectra extracted from two positions before flux stitching. At both points, the longest wavelength of NIRSpec and the shortest wavelength region of MIRI overlap with each other. While the ratio between median values is near unity at the center, it is much higher (>6) in the jet position. This discrepancy raises an issue in the JWST calibration pipeline that needs to be addressed.

Figure C4 shows the intensity ratio between the shortest wavelength range of MIRI and the longest wavelength range of NIRSpec. The NIRSpec image was resampled to match the pixel size of MIRI band 1. Although the ratio is below 2 in most images, it is significantly higher (~ 6) in some regions near the edges of the NIRSpec field. Notably, there is a 'blob' in the southeast corner where the ratio is elevated and overlaps with the blueshifted outflow jet.

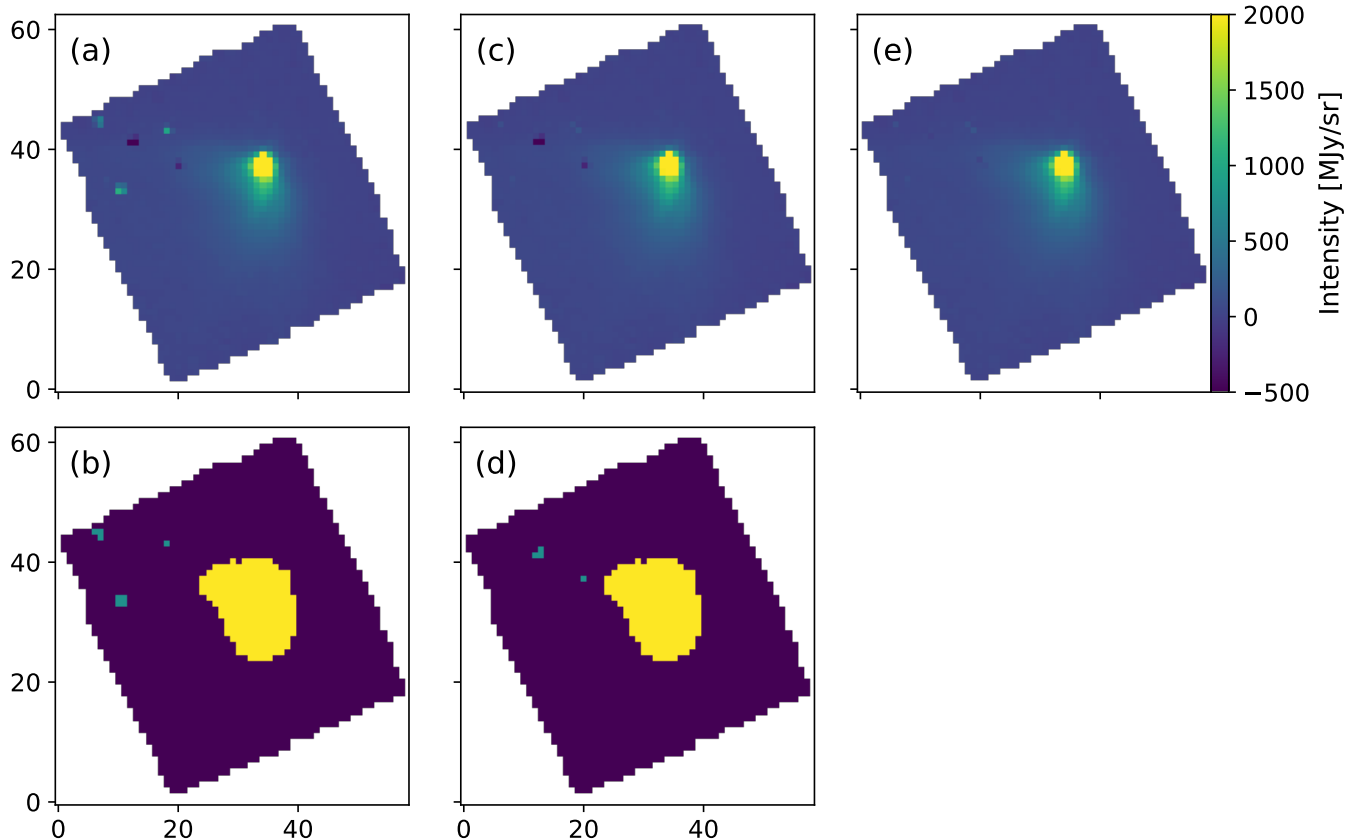


Figure B2. Hot and cold pixel subtraction process for the image slice at $2.7476\text{ }\mu\text{m}$. (a) Raw image slice. (b) ‘Sources’ detected by the `detect_sources` function. The yellow patch indicates the central source, while green pixels are detected as hot pixels. (c) Image after hot pixel flagging and median filtering. (d) Same with panel (b), but for cold pixels. (e) Final image slice, after correcting for cold pixels.

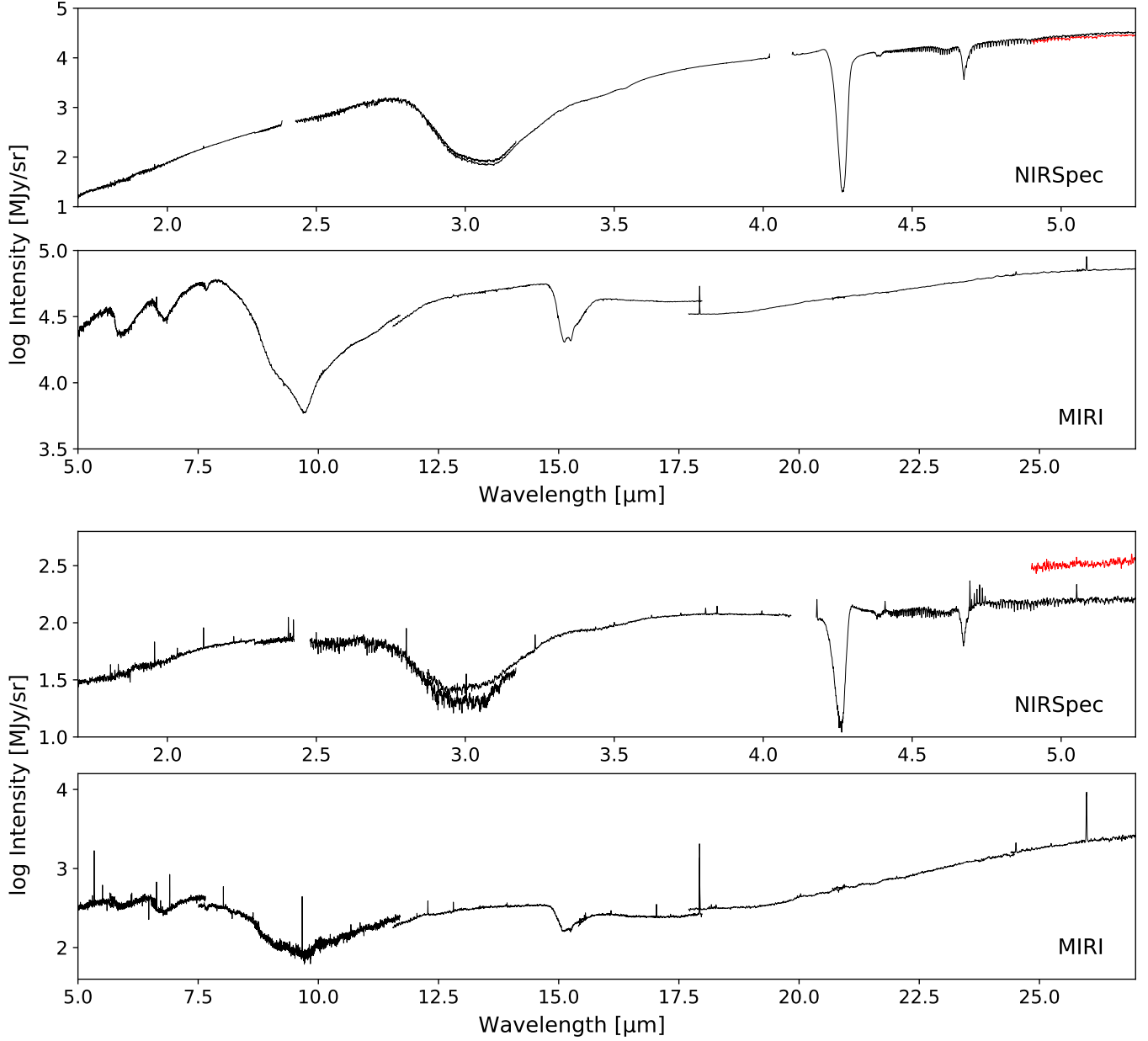


Figure C3. The upper two panels show spectra extracted from the ALMA continuum center using the aperture described in Section 2.2.1. The red spectrum on the top panel is the MIRI spectrum over the wavelength range that overlaps with NIRSpec. The lower two panels show the same comparison but for spectra extracted from the outflow position of Figure 1.

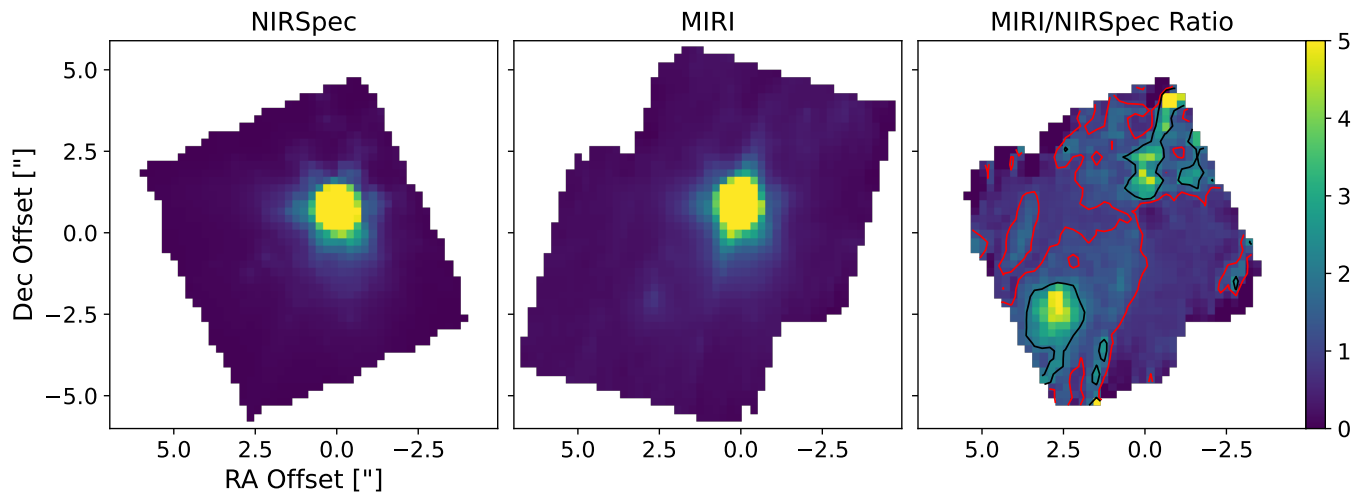


Figure C4. Median intensity maps between $5.0 \mu\text{m}$ and $5.2 \mu\text{m}$ for NIRSpec (left), MIRI (middle), and their ratio (right). In the ratio map, contours at values of 1 and 2 are drawn in red and black, respectively.

D. EMISSION LINE LIST

Table D1 lists the parameters of all observed H₂ lines, sorted by vibrational level. All data are taken from the HITRAN database (I. Gordon et al. 2026). Table D2 lists the parameters of all atomic lines detected in our data, sorted by species and wavelength. All data are taken from the NIST Atomic Spectra Database. For some lines, the Atomic Line List v3.00b5 (P. A. M. van Hoof 2018) reports slightly different wavelengths. Table A.1. of K. D. Assani et al. (2024) also presents a similar list of atomic lines and proposes that the two databases differ in their upper energy level (E_{up}) values. However, these differences arise solely from the use of different units: the NIST database uses cm⁻¹ as its energy unit, while the Atomic Linelist uses K. After converting the units (using $hc/k_B = 1.439$), the values from both databases are consistent.

E. H₂ EXCITATION DIAGRAM DESCRIPTION

E.1. *MCMC fitting*

For the excitation diagram analysis of H₂, we performed a Bayesian analysis using Markov-Chain Monte Carlo (MCMC) sampling with the publicly available python package `emcee` (D. Foreman-Mackey et al. 2013). We applied this to each pixel of the spatially convolved map. We assumed a Gaussian likelihood function, where the log-likelihood is proportional to $-\frac{1}{2}\chi^2$. The measurement uncertainties used to calculate χ^2 were derived from the Gaussian fit error of each line. We adopted uniform priors for the parameters within reasonable ranges: $15 < \log N [\text{cm}^{-2}] < 21$, $500 < T [\text{K}] < 2500$, and $5 < A_V < 30$. The same prior was used for fitting MIRI and NIRSpec data. We used 1000 walkers and 5000 steps, after the initial 1000 steps as burn-in. Figure E8 shows the marginalized posterior distributions in corner plots for the top panels of Figure 9, visualized with `corner.py` (D. Foreman-Mackey 2016). The posterior sampling converged well to a single value. The uncertainties of individual components are derived from the 16th and 84th percentiles of the posterior distribution.

E.2. *Effect of Extinction Curves in H₂ Excitation Diagram*

In Section 4.2, we adopted the extinction curve of K. M. Pontoppidan et al. (2024) to correct for the interstellar extinction since it is designed explicitly for dense molecular clouds with ice mantles. However, as N. L. Chapman et al. (2009) pointed out, extinction laws vary across different molecular clouds and environments due to variations in dust properties. K. D. Assani et al. (2025) also showed that grain growth in protostellar envelopes can change the extinction curve, deviating from

widely used relations. It is, therefore, important to check whether changing the assumed extinction curve significantly affects the results of the excitation diagram analysis.

If the extinction from the ambient material dominates over that from the protostellar envelope, it may be more appropriate to use the extinction curve of B. S. Hensley & B. T. Draine (2021), which characterizes the diffuse ISM, rather than that of K. M. Pontoppidan et al. (2024). Therefore, we repeated the excitation diagram analysis using the extinction curve of B. S. Hensley & B. T. Draine (2021). Figure E9 shows the results. For the long wavelengths, the distribution of column density and temperature is broadly consistent between the two models. However, the extinction values differ significantly, with those from B. S. Hensley & B. T. Draine (2021) approximately twice as large. Meanwhile, for the NIRSpec data, there is a significant increase in column density near the central source when using the extinction curve of B. S. Hensley & B. T. Draine (2021). This is because many H₂ lines in shorter wavelengths get affected by water ice absorption, which only K. M. Pontoppidan et al. (2024) takes into account.

Table D1. Spectral lines and parameters for H₂ emission lines detected in our observations.

Wavelength [μm]	Configuration	A _{ul} [s ⁻¹]	E _{up} [K]	g _{up}	spw
H ₂ 1–0					
1.8358	1–0 S(5)	3.95 (−7)	10341	45	235H
1.9576	1–0 S(3)	4.20 (−7)	8365	33	235H
2.0338	1–0 S(2)	3.98 (−7)	7584	9	235H
2.1218	1–0 S(1)	3.47 (−7)	6951	21	235H
2.2233	1–0 S(0)	2.52 (−7)	6471	5	235H
2.4066	1–0 Q(1)	4.29 (−7)	6149	9	235H
2.5000	1–0 Q(7)	2.34 (−7)	10341	45	235H
2.8025	1–0 O(3)	4.22 (−7)	6149	9	235H
3.0039	1–0 O(4)	2.89 (−7)	6471	5	235H, 395H
3.2350	1–0 O(5)	2.08 (−7)	6951	21	395H
3.5008	1–0 O(6)	1.50 (−7)	7584	9	395H
3.8074	1–0 O(7)	1.06 (−7)	8365	33	395H
H ₂ 0–0					
3.6262	0–0 S(15)	2.40 (−6)	21411	117	395H
3.7244	0–0 S(14)	1.99 (−6)	19403	33	395H
3.8461	0–0 S(13)	1.61 (−6)	17443	105	395H
3.9961	0–0 S(12)	1.27 (−6)	15540	29	395H
4.1811	0–0 S(11)	9.60 (−7)	13702	81	395H
4.4098	0–0 S(10)	7.01 (−7)	11940	25	395H
4.6946	0–0 S(9)	4.89 (−7)	10261	69	395H
5.0531	0–0 S(8)	3.23 (−7)	8677	21	395H
5.5112	0–0 S(7)	2.00 (−7)	7197	57	CH1-SHORT
6.1086	0–0 S(6)	1.14 (−7)	5830	17	CH1-MEDIUM
6.9095	0–0 S(5)	5.87 (−8)	4586	45	CH1-LONG
8.0250	0–0 S(4)	2.64 (−8)	3474	13	CH2-SHORT
9.6649	0–0 S(3)	9.83 (−9)	2504	33	CH2-MEDIUM
12.2786	0–0 S(2)	2.75 (−9)	1682	9	CH3-SHORT
17.0348	0–0 S(1)	4.76 (−10)	1015	21	CH3-LONG

NOTE—a(−b) indicates a×10^{−b}.

Table D2. Spectral lines and parameters for atomic lines detected in our observations.

Wavelength [μm]	Configuration	A _{ul} [s ⁻¹]	E _{up} [K]	g _{up}	spw
[Fe II]					
1.8094 ^a	a ⁴ F 7/2 – a ⁴ D 7/2	9.99 (−4)	11446	8	235H
4.8891	a ⁴ F 7/2 – a ⁶ D 7/2	9.3 (−5)	3496	8	395H
5.3401	a ⁴ F 9/2 – a ⁶ D 9/2	1.3 (−4)	2694	10	CH1-SHORT
6.7213	a ⁴ F 9/2 – a ⁶ D 7/2	1.16 (−5)	2694	10	CH1-LONG
17.936	a ⁴ F 7/2 – a ⁴ F 9/2	5.843 (−3)	3496	8	CH3-LONG, CH4-SHORT
24.5192	a ⁴ F 5/2 – a ⁴ F 7/2	3.934 (−3)	4083	6	CH4-LONG
25.9884	a ⁶ D 7/2 – a ⁶ D 9/2	2.151 (−3)	554	8	CH4-LONG
[Ne II]					
12.8135	2Po 1/2 – 2Po 3/2	8.59 (−3)	1123	2	CH3-SHORT
[Ni II]					
6.6360	² D 3/2 – ² D 5/2	5.54 (−2)	2168	4	CH1-LONG
10.6822	⁴ F 7/2 – ⁴ F 9/2	2.71 (−2)	13424	8	CH2-LONG

NOTE—a(−b) indicates a×10^{−b}.

^b The [Atomic Line List](#) reports the wavelength to be 1.8099 μm.

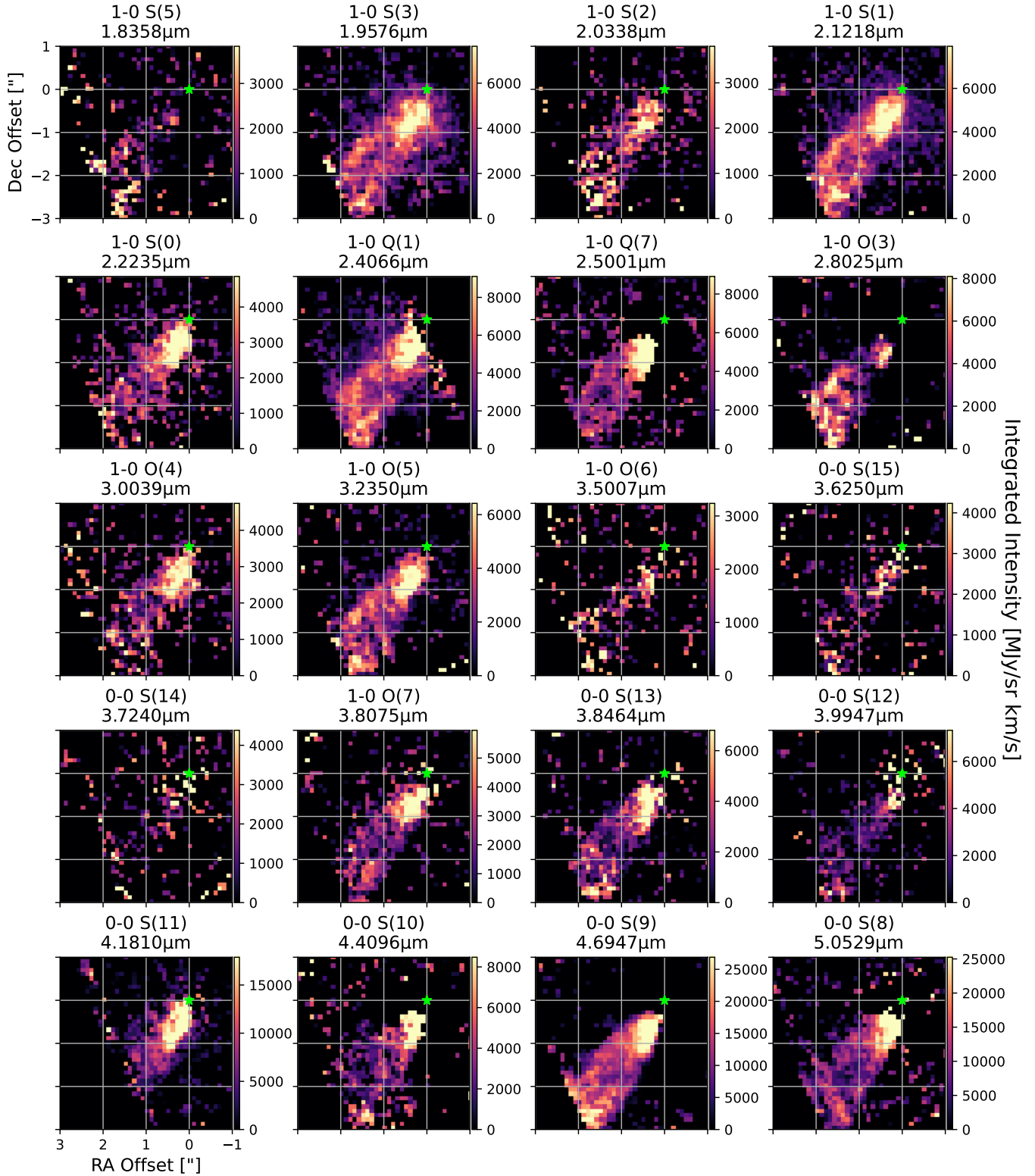


Figure D5. Integrated intensity maps of the H₂ lines detected with NIRSpec. The position of the central source is marked with a green star.

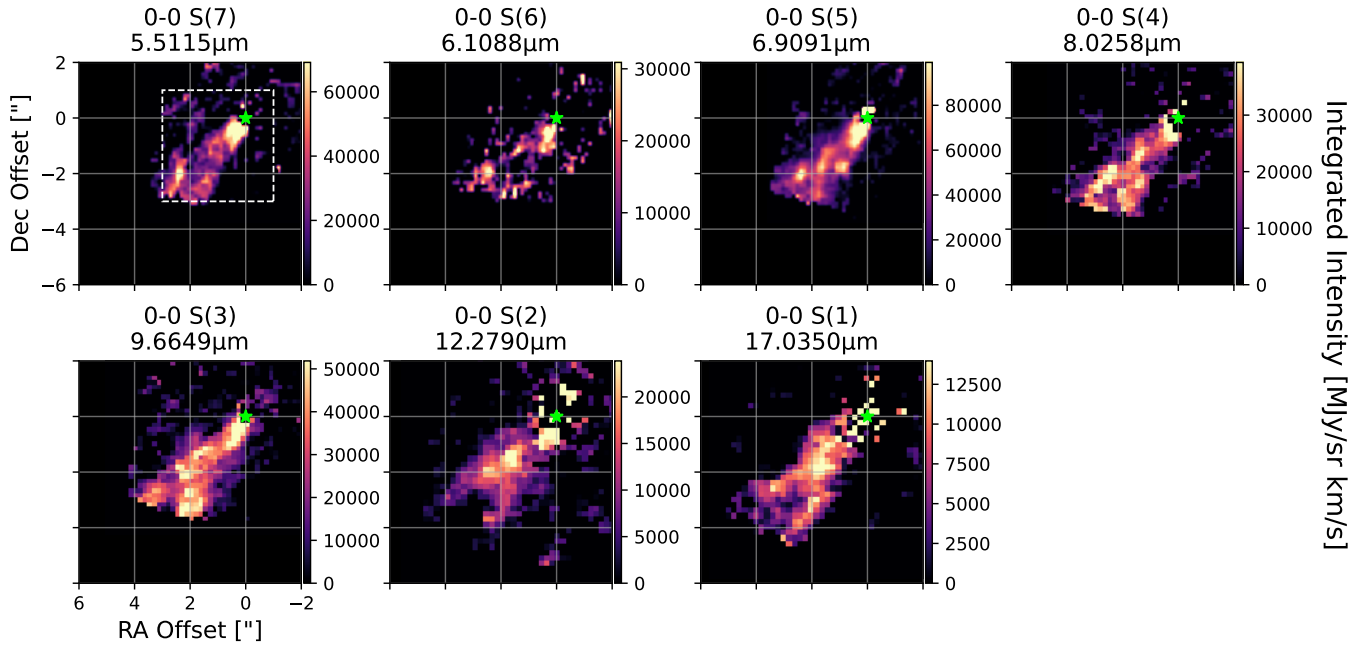


Figure D6. Integrated intensity maps of the H_2 lines detected with MIRI. The field of view of the NIRSpec data (Figure D5) is indicated by a white dashed square on the first panel.

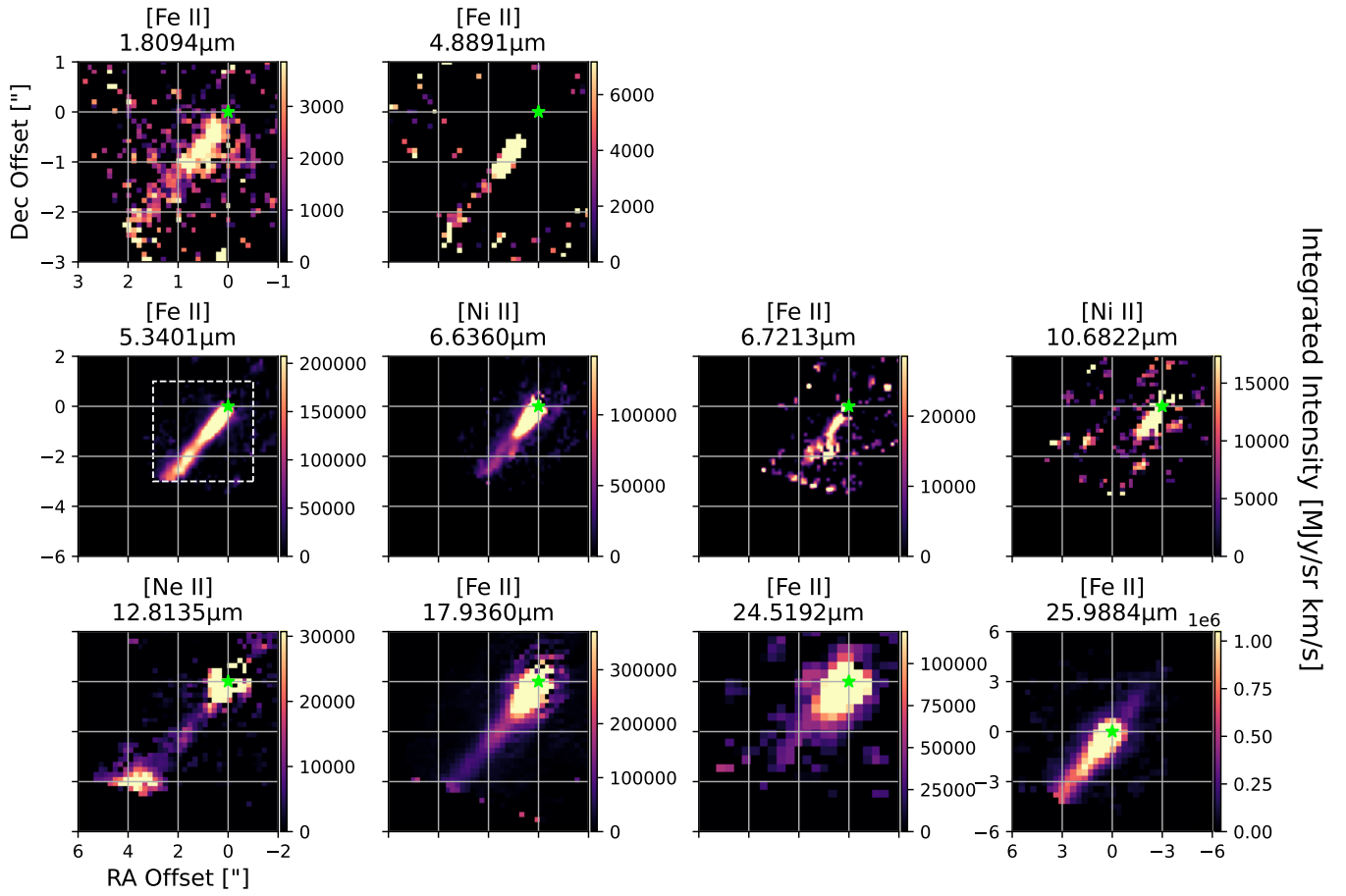


Figure D7. Integrated intensity maps of the detected atomic lines. The two transitions in the first row are from the NIRSpec wavelength range, while the remaining lines are from the MIRI range. A white dashed square on the first panel of the MIRI wavelength maps indicates the field of view of the NIRSpec data.

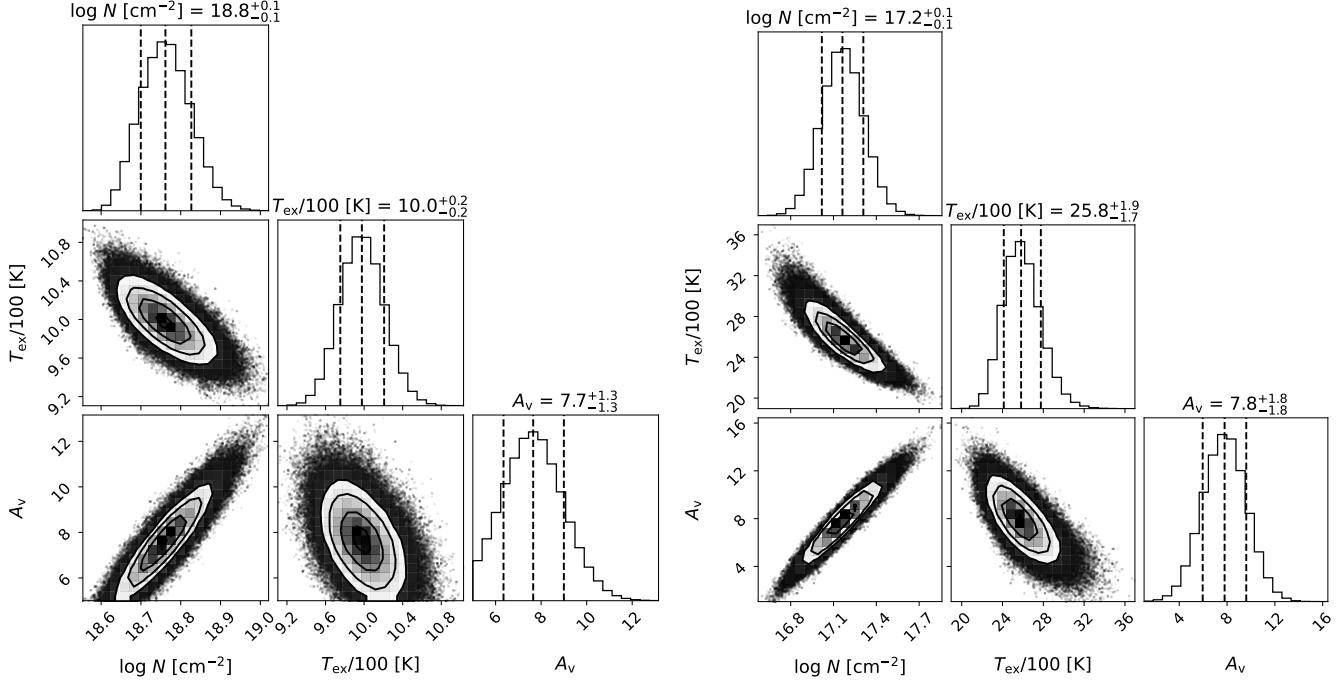


Figure E8. (left) Corner plot of the MCMC fit of Figure 9a. (right) Same with the left panel, but for Figure 9b.

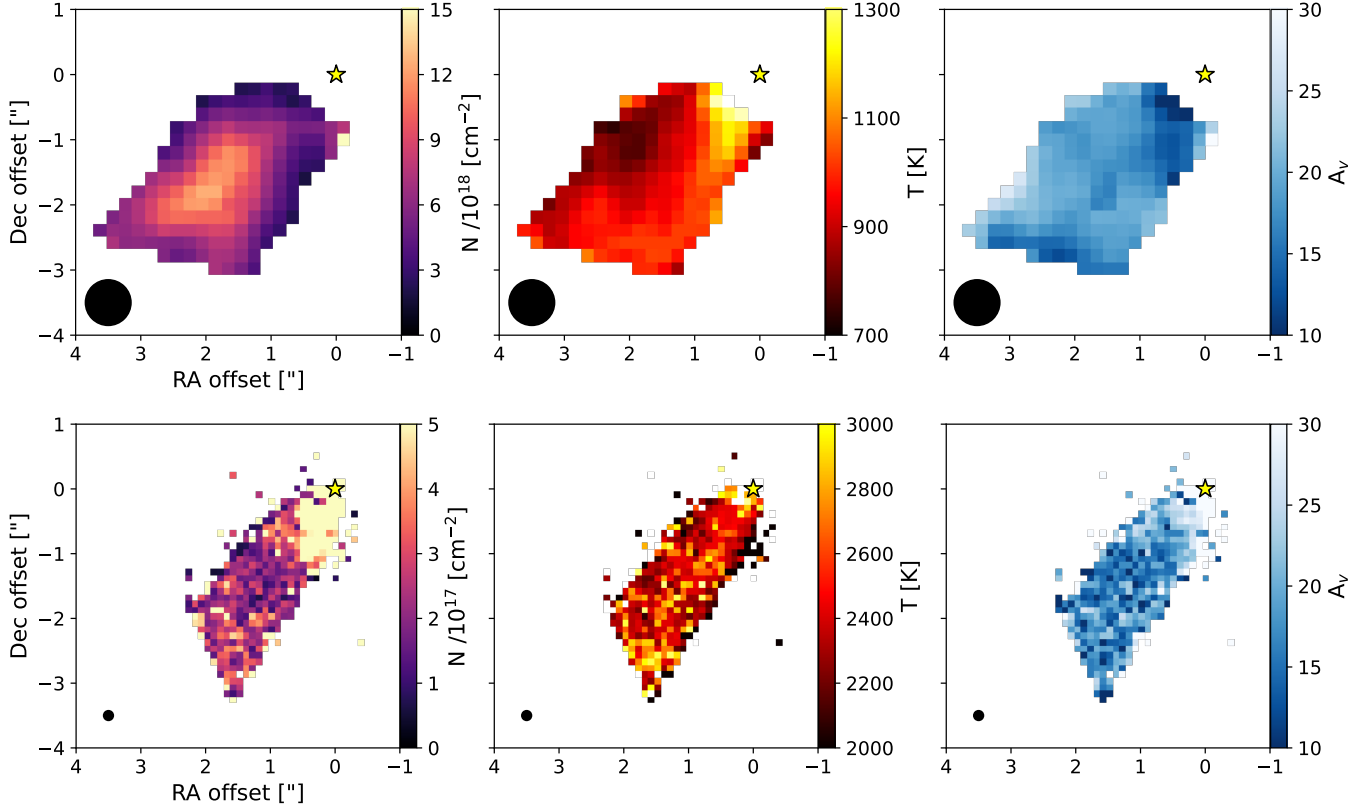


Figure E9. Same as the bottom 2 rows of Figure 9, but using the extinction curve of [B. S. Hensley & B. T. Draine \(2021\)](#).